Research Square

Preprints are preliminary reports that have not undergone peer review.
They should not be considered conclusive, used to inform clinical practice,
or referenced by the media as validated information.

Integrating machine learning with FEM-based CFD simulation of magneto-convective nanofluid flow through corrugated quadrantal cavity with a circular obstacle

Sadia Akter
Jagannath University
Md. Sarwar Alam
sarwar@math.jnu.ac.bd
Jagannath University
Md. Omar Faruk
Khulna University of Engineering & Technology

Article

Keywords: Corrugated cavity, natural convection, Cu-water nanofluid, finite element method, machine learning

Posted Date: November 3rd, 2026

DOI: https://doi.org/10.21203/rs.3.rs-11247529/v1

License: This work is licensed under a Creative Commons Attribution 4.0 International License.
Read Full License

Additional Declarations: No competing interests reported.

Integrating machine learning with FEM-based CFD simulation of magneto-convective nanofluid flow through corrugated quadrantal cavity with a circular obstacle

Sadia Akter[a], Md. Sarwar Alam[a*] and Md. Omar Faruk[b]

[a]Department of Mathematics, Jagannath University, Dhaka-1100, Bangladesh

[b]Department of Mechanical Engineering, Khulna University of Engineering & Technology, Khulna-9203, Bangladesh

[*]Email: sarwardu75@gmail.com

Abstract

Machine learning provides a data-driven approach to predicting complex heat transfer behaviour and to reducing the computational cost of numerical simulations of magnetohydrodynamic (MHD) nanofluid systems. This study develops a machine learning framework to predict the natural convective heat transfer mechanism inside a quarter-circular enclosure containing circular obstacle filled with Cu-H_2O nanofluid under an externally applied magnetic field. The coupled governing equations are solved using the finite element method for Rayleigh number (10^3-10^6), Hartmann number (0-100), and nanoparticle volume fractions (0.0-0.05). The effects of these parameters on flow structures and temperature distribution are investigated through streamlines, isotherms and average Nusselt number analyses. The results demonstrate that increasing Rayleigh number and nanoparticle concentration enhance heat transfer rate, whereas increasing Hartmann number reduces convective motion due to magnetic damping. A dataset comprising 151 numerical simulations is used to develop the predictive models based on XGBoost, CatBoost, random forest, and artificial neural network algorithms. The models are evaluated using five-fold cross validation, where CatBoost exhibits superior predictive performance with RMSE, MAE, MSE, and R^2 values of 0.0488 ± 0.0342, 0.0270 ± 0.0107, 0.0033 ± 0.0046, and 0.99883 ± 0.00186, respectively. Furthermore, SHAP analysis identifies Rayleigh number as the dominant parameter for predicting the average Nusselt number and reveals the nonlinear contribution of input variables to thermal performance. The proposed machine learning framework, coupled with finite element simulations, provides a reliable and interpretable approach to predicting heat transfer characteristics in MHD nanofluid systems while reducing the computational burden of conventional numerical analysis.

Keywords: Corrugated cavity, natural convection, Cu-water nanofluid, finite element method, machine learning.

Nomenclature

x, y	Dimensional coordinates
$\bar{x}$, $\bar{y}$	Dimensionless coordinates
u, v	Cartesian velocity components (m/s)
$\bar{u}$, $\bar{v}$	Non-dimensional velocity components
L	Enclosure length (m)
T	Temperature (K)
$\bar{T}$	Dimensionless temperature
T_h	Hot wall temperature (K)
T_c	Cold wall temperature (K)
p	Pressure (N/m^2)
$\bar{p}$	Dimensionless pressure
g	Gravitational acceleration (m/s^2)
Nu_{ave}	Average Nusselt number
Ra	Rayleigh number
Pr	Prandtl number
Ha	Hartmann number
B_0	Magnetic field
R^2	Coefficient of determination

Greek symbols

α	Thermal diffusivity (m^2/s)
β	Coefficient of thermal expansion (1/k)
k	Thermal conductivity (W/mK)
σ	Electrical conductivity
μ	Dynamic viscosity ($\mathrm{N \cdot s / m^2}$)
ν	Kinematic viscosity (m^2 / s)
ρ	Density
λ	Wavelength
ϕ	Nanoparticle volume fraction
ψ	Stream function

Abbreviation

MHD	Magnetohydrodynamic
CFD	Computational fluid dynamics
FEM	Finite Element Method
ML	Machine Learning
RF	Random Forest
XGBoost	eXtreme Gradient Boosting
CatBoost	Categorical Boosting
ANN	Artificial Neural Network
SHAP	SHapley Additive exPlanations
RMSE	Root mean square error
MAE	Mean absolute error
MSE	Mean squared error

Subscripts

nf	Nanofluid
np	Nanoparticles
bf	Base fluid
ave	Average

1. Introduction

Magnetohydrodynamic (MHD) natural convection in enclosures is widely studied for its relevance to nuclear reactor cooling, electronic and microelectronic devices, photovoltaic systems, solar technologies, and thermal management applications. In such configurations, thermal transport is governed by the interaction between buoyancy-driven fluid motion and the Lorentz force generated by an imposed magnetic field acting on the electrically conductive medium. Consequently, cavity geometry, buoyancy intensity, and magnetic-field strength strongly influence the fluid circulation and overall thermal transport behavior. Bawazeer and Alsoufi [1] investigated buoyancy-driven heat transfer inside a square enclosure using the finite element method (FEM) and reported enhanced heat transfer with increasing Rayleigh (Ra) and Prandtl (Pr) numbers. Rahman et al. [2] explored coupled thermal and concentration transport within a corrugated triangular domain with curved boundaries, whereas Aydin and Yesiloz [3] analyzed the effect of Ra on buoyancy-driven flow inside a quarter-circular cavity. Usman et al. [4] showed that Ra, Ha, and heat generation govern MHD flow and heat transfer in wavy enclosures. Further studies [5-7] demonstrated that enclosure geometry, buoyancy, and magnetic-field strength significantly govern MHD convection, with increasing Hartmann number (Ha) generally suppressing fluid circulation and convective heat transfer. Similar behavior was reported for non-Newtonian Casson fluids [8-9], where higher Ra intensified convection, whereas increasing Ha reduced flow strength and thermal transport.

Corrugated cavities have emerged as an effective passive technique for controlling buoyancy-driven convection by modifying recirculation zones, thermal boundary layers, and local temperature gradients. Aziz et al. [10] showed that corrugation and higher Ra enhanced thermal transport, while magnetic fields modified flow patterns in a corrugated semicircular porous MHD domain. Haq et al. [11] similarly reported improved thermal transport with increasing Ra and corrugation wavelength. Further investigations on porous corrugated enclosures [12-14] demonstrated that Ra, Ha, Darcy and Prandtl numbers, heat-source dimensions, and corrugation profiles collectively govern the resulting flow structure and overall thermal transport behavior.

Following the introduction of nanofluids by Choi [15], nanoparticle-enhanced fluids have been widely studied for thermal management applications due to their improved thermophysical properties. Islam et al. [16] investigated the effects of heat generation and absorption on Cu-H_2O nanofluid convection in a wavy triangular cavity using finite element analysis, highlighting the

role of nanoparticle properties and thermal parameters in enhancing heat transfer. Similarly, Dutta et al. [17] demonstrated the influence of cavity geometry on convective performance in a quarter-circular enclosure containing Cu-H_2O nanofluid. Studies on complex nanofluid filled configurations [18-21] further demonstrated that nanoparticle concentration, enclosure geometry, corrugated boundaries, internal obstacles, and magnetic fields significantly affect flow and heat transfer characteristics. Studies on finned and U-shaped porous nanofluid enclosures [22- 23] have shown that increasing Ra, Darcy number, nanoparticle loading, and geometrical modifications generally enhance heat transfer, whereas increasing Ha weakens convection. Similar findings for semicircular, obstacle-filled, trapezoidal, and wavy enclosures [24-27] confirmed that nanoparticle properties, obstacle geometry, wall configuration, buoyancy, and magnetic-field strength collectively control the thermal response.

Machine learning (ML) has emerged as a useful tool in thermal science, as it can effectively model nonlinear interactions among governing parameters while providing rapid predictions with considerably lower computational expense than repeated numerical simulations. Tumse et al. [28] used an ANN to predict the Nusselt number of CuO-water nanofluid flow in a magnetized grooved channel, achieving high accuracy ($R = 0.9988$) while reducing computation time from 8 h to 10 min. Topolnicki et al. [29] proposed a physics-informed CNN model for accurate porous media flow prediction with enhanced computational efficiency, while Ali et al. [30] proposed a CFD-ANN model for accurate prediction of hydrodynamic forces in non-Newtonian flows with reduced computational time. Subsequent studies [31-35] combined CFD or FEM simulations with machine learning to predict flow and heat transfer in complex systems involving MHD, nanofluids, porous media, and non-spherical particles demonstrating high predictive accuracy with limited numerical data. Bawazeer et al. [36] developed ML models for predicting the Nusselt number in a fin-enhanced square cavity, while Reddy et al. [37] coupled CFD and ML to predict heat transfer and entropy generation in a partially porous cavity. Further studies [38-40] have advanced data-driven thermal analysis through ML-based prediction of thermal performance, CFD-neural network approaches for evaluating hybrid nanofluid thermo-fluid behavior, FEM-XGBoost modeling of Nusselt number in three-dimensional MHD enclosures, and SHAP-based explainability for developing interpretable and physics-consistent heat transfer models.

Despite substantial progress in MHD nanofluid heat transfer research, several aspects remain insufficiently explored. Previous investigations have largely concentrated on conventional cavity

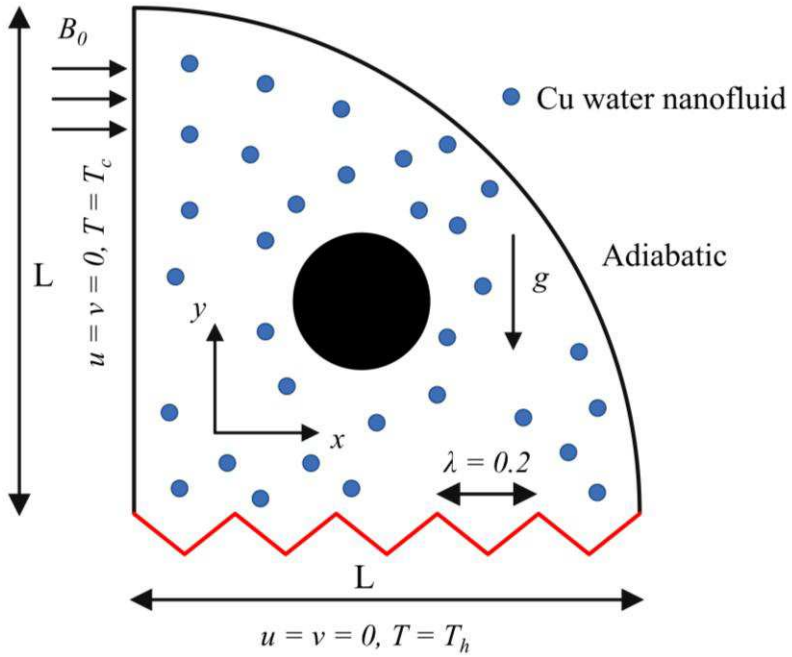
configurations or individual geometric modifications, including corrugated surfaces, internal obstacles, and nanoparticle incorporation. However, the combined impact of a corrugated quadrantal cavity and an insulated circular obstacle on MHD natural convection remains unclear. Furthermore, while machine learning (ML) methods have shown considerable potential for predicting complex thermal behaviours, their integration with geometrically intricate MHD nanofluid systems has received limited attention. These limitations highlight the need for a comprehensive investigation into the coupled effects of buoyancy, magnetic field intensity, nanoparticle concentration, and cavity geometry, along with the development of interpretable data-driven models for reliable thermal prediction.

To address the limitations identified in previous studies, this work investigates magnetically influenced, buoyancy-driven heat transfer of a Cu-H_2O nanofluid within a two-dimensional corrugated quadrantal cavity containing an insulated circular obstacle, using the Galerkin weighted residual finite element method. A CFD-generated dataset comprising 151 samples, obtained by varying the Rayleigh number (Ra), Hartmann number (Ha), and nanoparticle volume fraction (ϕ), is utilized to train and evaluate XGBoost, CatBoost, Random Forest, and Artificial Neural Network models for predicting the average Nusselt number. The predictive performance of these models is evaluated using R^2, RMSE, MAE, and MSE, while SHAP (Shapley Additive Explanations) analysis is employed to interpret model predictions and quantify the contribution of individual governing parameters to the thermal response. This integrated CFD-ML framework provides an efficient and interpretable approach to predicting and understanding heat transfer behaviour in complex MHD nanofluid systems.

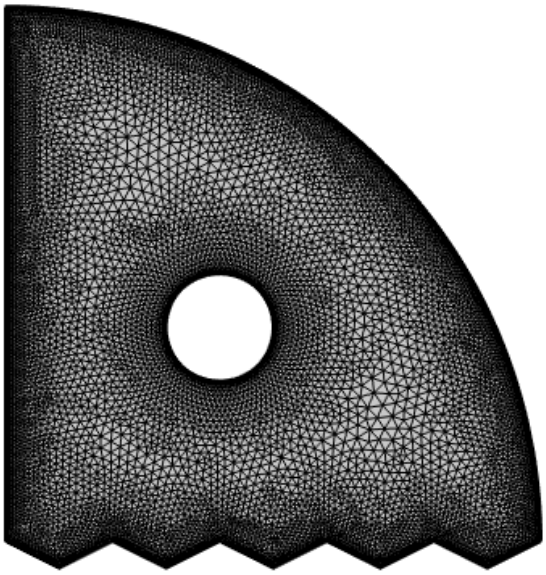
2. Physical Configuration and Theoretical Modeling

2.1 Geometry of the Computational Domain

The schematic diagram of the physical model considered in this study is depicted in Figure 1(a). A quarter-circular computational domain with a characteristic length (L) is considered, and Cu-water nanofluid is used as the working fluid. The corrugated lower boundary is subjected to a uniform hot temperature (T_h), whereas a lower temperature (T_c) is prescribed along the vertical boundary. The curved boundary is thermally insulated (adiabatic). A uniform gravitational acceleration acts vertically downward, inducing buoyancy-driven natural convection throughout the computational domain.



(a)



(b)

Figure 1: Schematic representation of the computational model: (a) physical domain with the imposed boundary conditions and (b) corresponding grid distribution.

Additionally, a constant magnetic field B_0 is imposed in the (x)-direction, generating a Lorentz force that influences the fluid motion. All solid boundaries satisfy the no-slip condition ($u = v = 0$

). Steady, laminar, two-dimensional, and incompressible flow conditions are considered. Figure 1(b) illustrates the grid distribution employed in the computational domain. The nanofluid is modeled as a homogeneous Newtonian medium with invariant thermophysical properties, while density changes associated with the buoyancy force are incorporated according to the Boussinesq hypothesis. Thermal radiation, viscous dissipation, Joule heating, magnetic induction, Brownian diffusion, and thermophoretic effects are disregarded in the present analysis.

2.2 Physical and Thermal Properties of Nanofluids

Nanofluids consist of nanoscale particles dispersed within conventional base fluids to improve their thermal transport performance. By dispersing nanoscale solid particles in a base fluid, the effective thermal conductivity, heat capacity, and convective heat transfer can be significantly improved. Among various nanofluids, the Cu-water nanofluid has been widely studied for its superior heat transfer performance. In this study, a Cu-water nanofluid is considered, with water as the base fluid and copper as the nanoparticle phase. The nanoparticles are spherical with a diameter of $20-30\ nm$, which is commonly adopted in numerical and experimental studies to ensure stable suspension and reliable thermophysical behavior.

Table 1: Physical Properties of H_2O and Cu Nanoparticles [16].

Property	H_2O	Cu
$k(W/mK)$	0.613	401
$\rho(kg/m^3)$	997.1	8954
$\beta(K^{-1})$	2.1×10^{-4}	1.67×10^{-5}
$C_p(J/kgK)$	4179	383
$\mu(kg/ms)$	8.91×10^{-5}	–

The high thermal conductivity of copper ($\approx 401\ Wm^{-1}K^{-1}$) significantly enhances the heat transfer capability of the base fluid. Cu-water nanofluid is also favored for its thermal stability, chemical compatibility with water, cost-effectiveness, and extensive literature validation, making it suitable

for natural convection and other thermal management applications. The thermophysical properties of copper and water considered in this analysis are listed in Table 1.

2.3 Mathematical Model

The enclosure is assumed to contain a steady, laminar, incompressible Cu-water nanofluid with uniform thermophysical properties. Density variations are considered only in the buoyancy term following the Boussinesq approximation, while effects of radiation, viscous dissipation, Joule heating, induced magnetic fields, Brownian motion, and thermophoresis are neglected. Under these conditions, the flow and heat transfer are described by the dimensional continuity, momentum, and energy equations for laminar natural convection under an external magnetic field.

$$\frac{\partial u}{\partial x}+\frac{\partial v}{\partial y}=0 \tag{1}$$

$$\rho_{nf}(u\frac{\partial u}{\partial x}+v\frac{\partial u}{\partial y})=-\frac{\partial p}{\partial x}+\mu_{nf}(\frac{\partial^2 u}{\partial x^2}+\frac{\partial^2 u}{\partial y^2}) \tag{2}$$

$$\rho_{nf}(u\frac{\partial v}{\partial x}+v\frac{\partial v}{\partial y})=-\frac{\partial p}{\partial y}+\mu_{nf}(\frac{\partial^2 v}{\partial x^2}+\frac{\partial^2 v}{\partial y^2})+(\rho\beta)_{nf}g(T-T_c)-\sigma_{nf}{B_0}^2 v \tag{3}$$

$$u\frac{\partial T}{\partial x}+v\frac{\partial T}{\partial y}=\alpha_{nf}(\frac{\partial^2 T}{\partial x^2}+\frac{\partial^2 T}{\partial y^2}) \tag{4}$$

In the governing equations, u and v denote the velocity components in the x- and y-directions, respectively, while p and T represent the fluid pressure and temperature fields. The parameters β and B_0 correspond to the thermal expansion coefficient and the strength of the externally applied magnetic field, respectively. The boundary conditions corresponding to the present physical configuration are specified as follows:

At the vertical cold wall: $u=0, v=0, T=T_c$

At the corrugated heated wall: $u=0, v=0, T=T_h$ (5)

At the inclined adiabatic wall: $u=0, v=0, n.\nabla T=0$

where n represents the unit normal vector to the boundary surface.

The thermo-physical properties of the nanofluid, including its effective density ρ_{nf}, are defined as follows:

$$\rho_{nf}=\phi\rho_{np}+(1-\phi)\rho_{bf} \tag{6}$$

and ϕ represents the fraction of nanoparticles dispersed within the base fluid. Additionally, the thermal diffusivity of the nanofluid, denoted as α_{nf}, can be expressed as:

$$\alpha_{nf} = \frac{k_{nf}}{(\rho C_p)_{nf}} \tag{7}$$

The nanofluid's heat capacitance $(\rho C_p)_{nf}$ is given by

$$(\rho C_p)_{nf} = \phi(\rho C_p)_{np} + (1-\phi)(\rho C_p)_{bf} \tag{8}$$

In addition, the thermal expansion coefficient of the nanofluid, $(\rho\beta)_{nf}$, is formulated as

$$(\rho\beta)_{nf} = \phi(\rho\beta)_{np} + (1-\phi)(\rho\beta)_{bf} \tag{9}$$

Also, the electrical conductivity of the nanofluid is, σ_{nf}, is determined using

$$\sigma_{nf} = \phi\sigma_{np} + (1-\phi)\sigma_{bf} \tag{10}$$

Furthermore, the dynamic viscosity of the nanofluid, μ_{nf}, accounting for the nanoparticle fraction, is described using Brinkman's model [41]:

$$\mu_{nf} = \frac{\mu_{bf}}{(1-\phi)^{2.5}} \tag{11}$$

The effective thermal conductivity of the nanofluid, k_{nf}, is calculated using the Maxwell model [42]:

$$k_{nf} = k_{bf}\left[\frac{(k_{np} + 2k_{bf}) - 2\phi(k_{bf} - k_{np})}{(k_{np} + 2k_{bf}) + \phi(k_{bf} - k_{np})}\right] \tag{12}$$

Here, k_{np} and k_{bf} denote the thermal conductivities of the nanoparticles and the base fluid, respectively.

The governing equations (1) - (4) together with the boundary conditions in Eq. (5) are transformed into dimensionless form by introducing the following nondimensional variables:

$$\bar{x} = \frac{x}{L},\ \bar{y} = \frac{y}{L},\ \bar{u} = \frac{uL}{\alpha_{bf}},\ \bar{v} = \frac{vL}{\alpha_{bf}},\ \bar{p} = \frac{pL^2}{\rho_{nf}\alpha_{bf}{}^2},\ \bar{T} = \frac{T - T_c}{T_h - T_c}$$

The corresponding dimensionless parameters are defined as:

$$Ra = \frac{\beta_{bf} g L^3 (T_h - T_c)}{\upsilon_{bf}\alpha_{bf}},\ \mathrm{Pr} = \frac{\upsilon_{bf}}{\alpha_{bf}},\ Ha = B_0 L\sqrt{\frac{\sigma_{nf}}{\rho_{nf}\upsilon_{bf}}}$$

Where $\bar{x}$ and $\bar{y}$ are the dimensionless coordinates in the horizontal and vertical directions, respectively; $\bar{u}$ and $\bar{v}$ are the dimensionless velocity components; $\bar{p}$ is the dimensionless

pressure; and $\overline{T}$ is the dimensionless temperature. Here, Ra, $\Pr$, and Ha represent the Rayleigh number, Prandtl number, and Hartmann number, respectively.

After substituting the dimensionless variables into the governing equations, the dimensionless transport equations can be written as follows:

$$\frac{\partial \overline{u}}{\partial \overline{x}} + \frac{\partial \overline{v}}{\partial \overline{y}} = 0 \tag{13}$$

$$\overline{u}\frac{\partial \overline{u}}{\partial \overline{x}} + \overline{v}\frac{\partial \overline{u}}{\partial \overline{y}} = -\frac{\rho_f}{\rho_{nf}}\frac{\partial \overline{p}}{\partial \overline{x}} + \Pr\frac{\upsilon_{nf}}{\upsilon_f}\left(\frac{\partial^2 \overline{u}}{\partial \overline{x}^2} + \frac{\partial^2 \overline{u}}{\partial \overline{y}^2}\right) \tag{14}$$

$$\overline{u}\frac{\partial \overline{v}}{\partial \overline{x}} + \overline{v}\frac{\partial \overline{v}}{\partial \overline{y}} = -\frac{\rho_f}{\rho_{nf}}\frac{\partial \overline{p}}{\partial \overline{y}} + \Pr\frac{\upsilon_{nf}}{\upsilon_f}\left(\frac{\partial^2 \overline{v}}{\partial \overline{x}^2} + \frac{\partial^2 \overline{v}}{\partial \overline{y}^2}\right) + Ra\Pr\frac{(\rho\beta)_{nf}}{\rho_{nf}\beta_f}\overline{T} - Ha^2\Pr\overline{v} \tag{15}$$

$$\overline{u}\frac{\partial \overline{T}}{\partial \overline{x}} + \overline{v}\frac{\partial \overline{T}}{\partial \overline{y}} = \frac{\alpha_{nf}}{\alpha_f}\left(\frac{\partial^2 \overline{T}}{\partial \overline{x}^2} + \frac{\partial^2 \overline{T}}{\partial \overline{y}^2}\right) \tag{16}$$

The dimensionless boundary conditions for the present physical model are specified as follows:

At the vertical cold wall: $\overline{u} = 0, \overline{v} = 0, \overline{T} = 0$

At the corrugated heated wall: $\overline{u} = 0, \overline{v} = 0, \overline{T} = 1$ (17)

At the inclined adiabatic wall: $u = 0, v = 0, n.\nabla \overline{T} = 0$

The heat transfer performance is expressed in terms of the average Nusselt number. For the heated wall, the average Nusselt number (Nu_{ave}) is calculated using the following expression:

$$Nu_{ave} = -\left(\frac{k_{nf}}{k_f}\right)\frac{1}{L_s}\int_0^{L_s}\frac{\partial \overline{T}}{\partial n}dS \tag{18}$$

where L_s denotes the length of the corrugated heated surface, and n represents the unit normal vector to the surface.

3. Numerical Methodology

3.1 Computational Procedure

The non-dimensional governing equations (13) – (16) are solved using the Galerkin weighted residual finite element method (FEM) subject to the prescribed initial and boundary conditions (17). The computational domain is discretized into a finite number of irregular elements, within which the dependent variables are approximated using appropriate interpolation functions. The

Galerkin weighted residual formulation is then employed to obtain the corresponding elemental equations, which are subsequently assembled into a global system of nonlinear algebraic equations. The Newton-Raphson iteration scheme is employed to solve the resulting nonlinear system using MATLAB. The iterative procedure is continued until the convergence criterion $\left|\Gamma^{n+1}-\Gamma^{n}\right| \le 10^{-6}$ is satisfied, where n and $n+1$ denote two successive iterations, and Γ represents the velocity components, pressure, and temperature.

3.2 Grid Independency Test

A grid independence test is carried out to verify that the numerical results of the present model are not significantly influenced by mesh resolution. For the Cu-water nanofluid, the test is performed for $Ra = 10^4$, $Ha = 20$, $\phi = 0.05$, and $\mathrm{Pr} = 6.2$. The results are summarized in Table 2 and Figure 2. Nine successive mesh resolutions ranging from extremely coarse to extremely fine are examined here. The corresponding degrees of freedom (DoF) increases from 1370 to 98117. It is observed that the average Nusselt number gradually increases with increasing DoF and approaches a nearly constant value at higher mesh resolutions. The extra fine mesh contains 78533 DoF and 17843 elements with $Nu_{ave} = 3.6796$, whereas further refinement to 98117 DoF and 22739 elements for the extremely fine mesh changes Nu_{ave} only to 3.6797. The difference between these two values is only 0.0001.

Table 2: Grid independency test at $Ra = 10^4$, $Ha = 20$, $\mathrm{Pr} = 6.2$ and $\phi = 0.05$.

Mesh Type	DoF	Number of Elements	Nu_{ave}
Extremely coarse	1370	238	2.3511
Extra coarse	2466	446	2.5557
Coarser	3557	683	2.5966
Coarse	6240	1252	2.7805
Normal	8048	1660	2.8219
Fine	11880	2530	2.9516
Finer	29096	6350	3.3489
Extra fine	78533	17843	3.6796
Extremely fine	98117	22739	3.6797

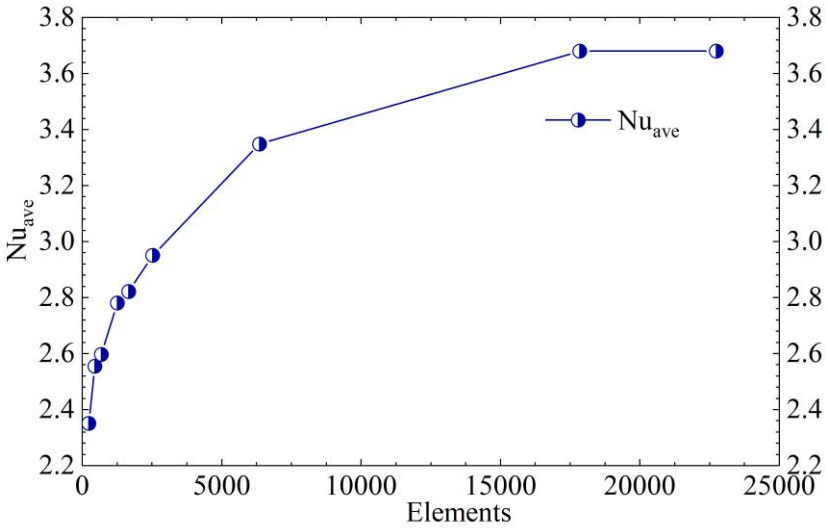


Figure 2: Variation of the average Nusselt number with the number of elements.

This small variation indicates that further refinement has almost no effect on the average Nusselt number. Therefore, the extra fine mesh is selected for the subsequent numerical simulations.

3.3 Code Validation

The present numerical code was validated against the results reported by Dutta et al. [17] by comparing the average Nusselt number, streamlines, and isotherms for different Hartmann numbers at $Ra = 10^3$, $\Pr = 6.2$, and $\phi = 0.05$. Table 3 shows that the predicted average Nusselt numbers remain very close to the reference values, with the maximum deviation limited to 1.784%. This small discrepancy indicates that the present formulation accurately evaluates the overall heat transfer rate. The streamline and isotherm contours obtained in the present study are compared with those of Dutta et al. [17] in Figure 3, showing close agreement over the considered range of Ha. The gradual weakening of the flow and the smoother temperature contours with increasing Ha suggest that the magnetic field suppresses fluid motion and makes heat transfer more conduction dominated. Moreover, the gradual reduction in circulation strength with increasing Hartmann number is consistently captured in both sets of results. Overall, the close agreement with the benchmark results confirms the accuracy and suitability of the present numerical scheme for the subsequent analysis.

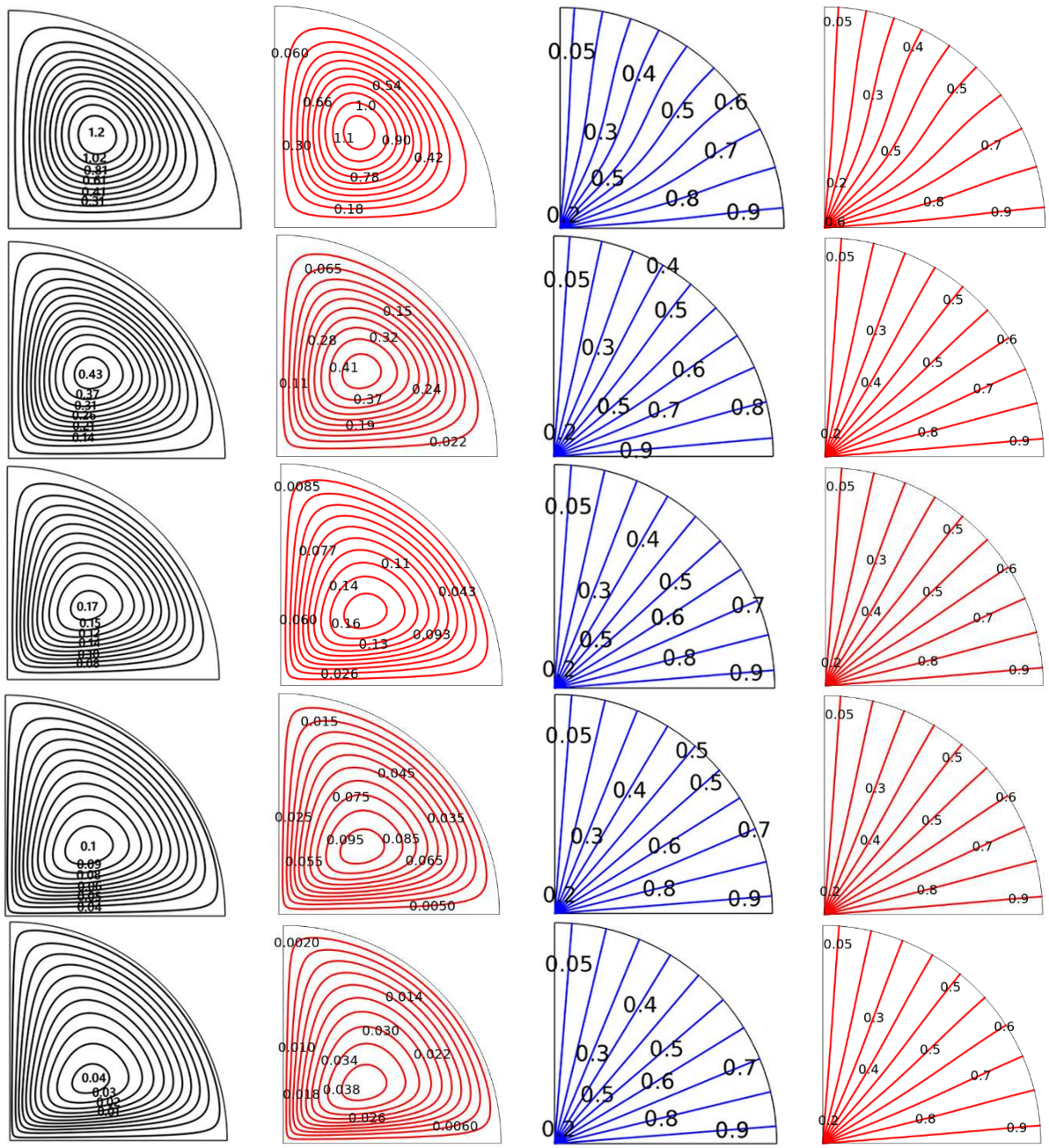


Figure 3: Comparison between Dutta et al. [17] and the present study for $Ra = 10^3$, $\phi = 0.05$, and $\Pr = 6.2$: (a-b) streamlines, (c-d) isotherms. The rows from top to bottom represent $Ha = 0, 20, 40, 60$, and 100 respectively.

Table 3: Comparison of average Nusselt number (Nu_{ave}) with Dutta et al. [17] for different Ha at $Ra = 10^3$, Pr = 6.2 , and $\phi = 0.05$.

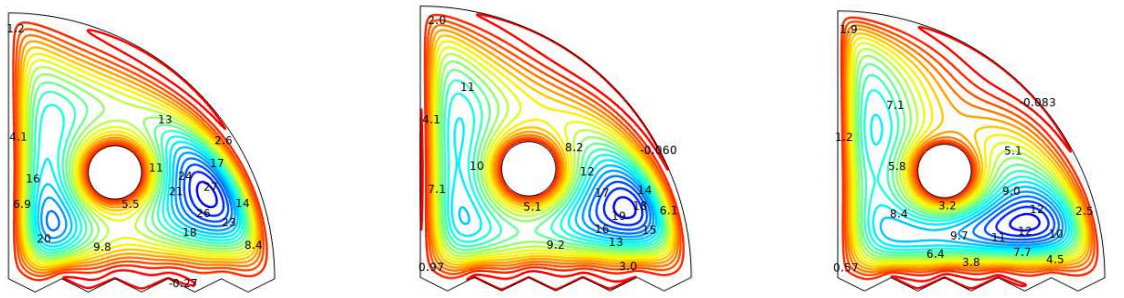
Ha	Nu_{ave}		Error (%)
	Dutta et al. [17]	Present Study	
0	4.501	4.581	1.777
20	4.486	4.565	1.761
40	4.484	4.564	1.784
60	4.484	4.564	1.784
80	4.484	4.564	1.784
100	4.484	4.564	1.784

4. Results and Discussion

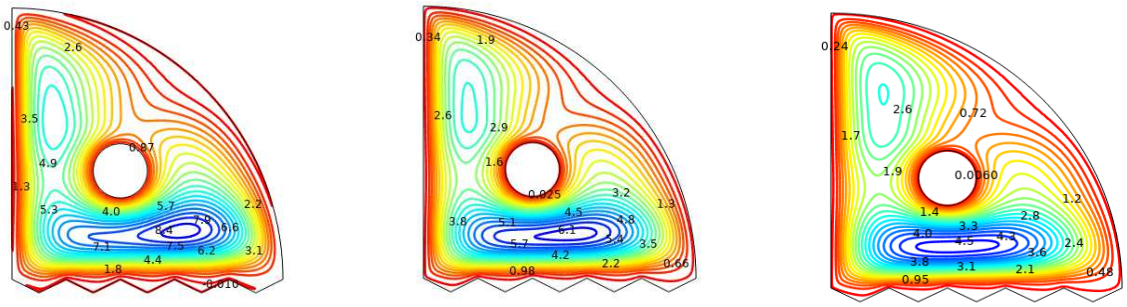
Numerical simulations are performed to examine the effects of Rayleigh number (Ra), Hartmann number (Ha), and nanoparticle volume fraction (ϕ) on MHD natural convective heat transfer in a corrugated quarter-circular cavity filled with Cu-H_2O nanofluid and containing an insulated circular obstacle. The resulting flow and thermal characteristics are analyzed in terms of streamlines, isotherms, and the average Nusselt number Nu_{ave}, while the Prandtl number is kept constant throughout the computations. The influence of these governing parameters on the flow and thermal fields is discussed in the following subsections.

4.1. Effect of Hartmann number

Figures 4 and 5 illustrate the influence of the Hartmann number $(Ha = 0 - 100)$ on the flow and thermal fields at $Ra = 10^6$ and $\phi = 0.05$. As shown in Figure 4, at $Ha = 0$, strong buoyancy-driven circulation is observed, with the dominant vortex developing on the right side of the circular obstacle. The maximum stream function magnitude, $|\psi|_{\max}$, decreases markedly from approximately 27 at $Ha = 0$ to 19, 12, 8.4, 6.1, and 4.5 at $Ha = 20$, 40, 60, 80, and 100 respectively. Thus, increasing Ha from 0 to 100 reduces $|\psi|_{\max}$ by approximately 83.3%, quantitatively confirming the strong suppression of fluid circulation. Moreover, the primary vortex gradually shifts toward the lower region and becomes increasingly elongated as the magnetic field strengthens.

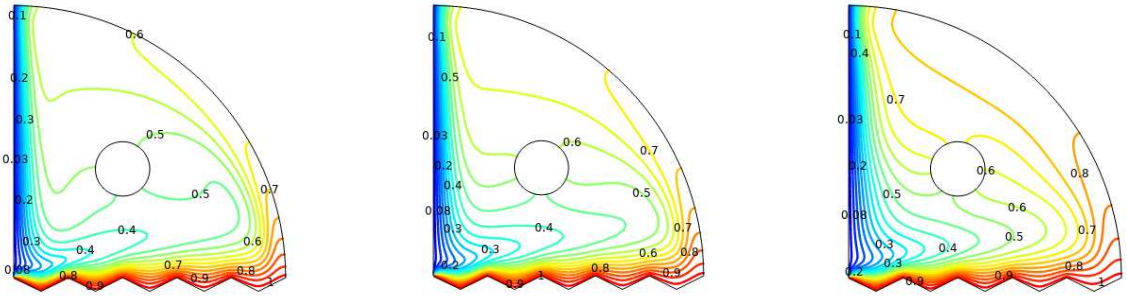


$Ha = 0$ $Ha = 20$ $Ha = 40$

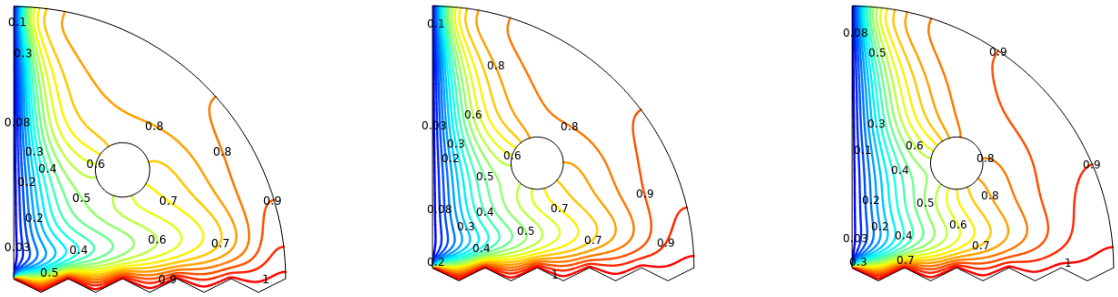


$Ha = 60$ $Ha = 80$ $Ha = 100$

Figure 4: Effect of different Ha values on streamline distributions at $Ra = 10^6$ and $\phi = 0.05$.



$Ha = 0$ $Ha = 20$ $Ha = 40$



$Ha = 60$ $Ha = 80$ $Ha = 100$

Figure 5: Effect of various values of Ha on isotherm distributions at $Ra = 10^6$ and $\phi = 0.05$.

This behavior results from the enhanced Lorentz force, which opposes the buoyancy-induced motion and dissipates momentum, thereby weakening convective circulation. The corresponding isotherm distributions in Figure 5 exhibit a consistent thermal response. At low Ha, the isotherms are strongly distorted, particularly near the corrugated heated wall and around the circular obstacle, indicating vigorous convective transport. With increasing Ha, the contours become progressively smoother and more regularly distributed. At $Ha = 80-100$, the reduced distortion of the isotherms indicates substantially weaker thermal mixing and an increasing dominance of conduction. Therefore, both the qualitative evolution of the flow and temperature fields and the approximately 83% reduction in $|\psi|_{max}$ demonstrate that increasing the Hartmann number effectively suppresses buoyancy-driven convection and consequently weakens convective heat transfer.

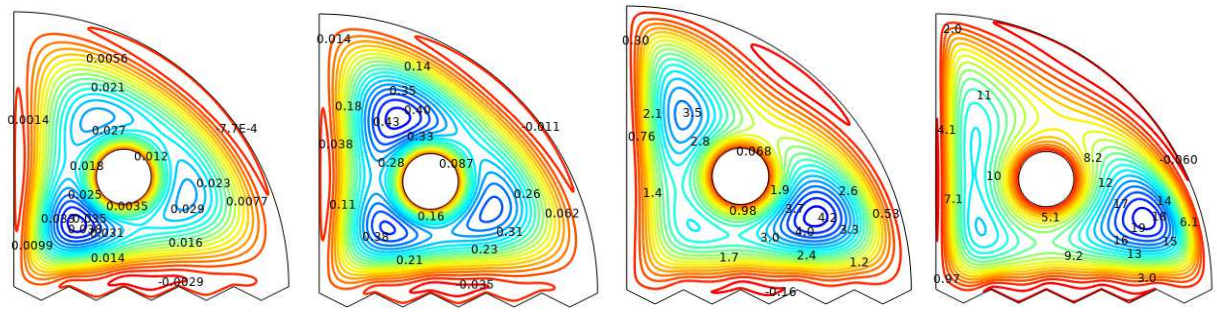


Figure 6: Streamline patterns for multiple Ra values at $Ha = 20$ and $\phi = 0.05$.

4.2. Effect of Rayleigh Number

The evolution of the flow and thermal fields over the range $Ra = 10^3 - 10^6$ is depicted in Figures 6 and 7 at $Ha = 20$ and $\phi = 0.05$. As shown in Figure 6, the flow is relatively weak at $Ra = 10^3$, with small recirculation zones forming around the circular obstacle. Increasing Ra substantially intensifies the fluid motion and promotes the development of stronger, well-defined vortical structures. The maximum stream function magnitude, $|\psi|_{max}$, rises from approximately 0.038 at $Ra = 10^3$ to 0.43, 4.2, and 19 at $Ra = 10^4, 10^5$, and 10^6, respectively. Relative to $Ra = 10^3$, the corresponding flow strengths are approximately 11.3, 110.5, and 500 times greater. At $Ra = 10^5$ and $Ra = 10^6$, the right-side vortex becomes increasingly dominant, while the left circulation expands along the vertical wall. This pronounced enhancement results from the increasing dominance of buoyancy forces over viscous resistance and magnetic damping.

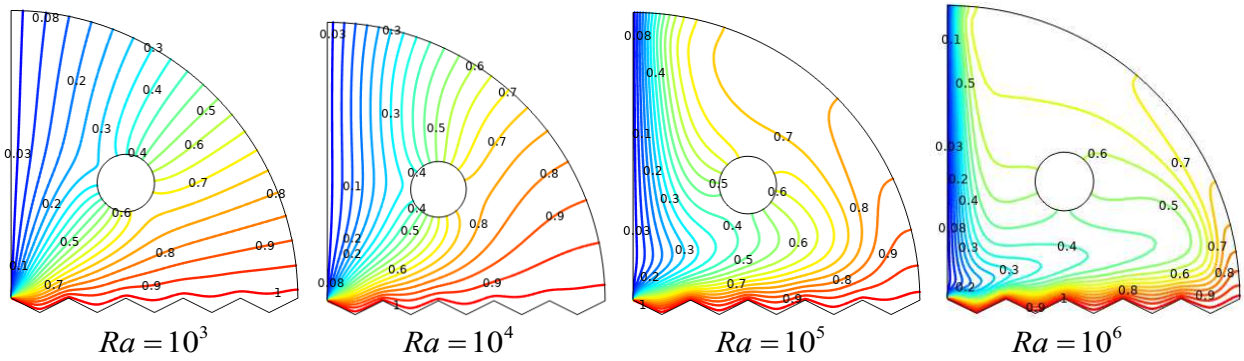
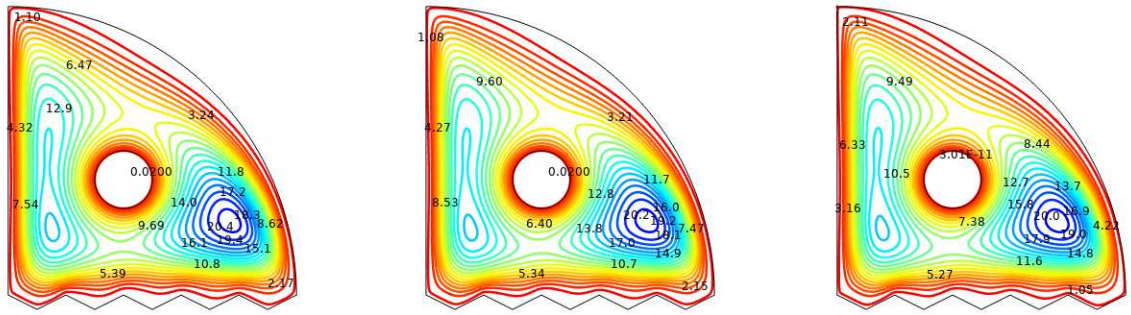


Figure 7: Isotherm patterns for varying Ra values at $Ha = 20$ and $\phi = 0.05$.

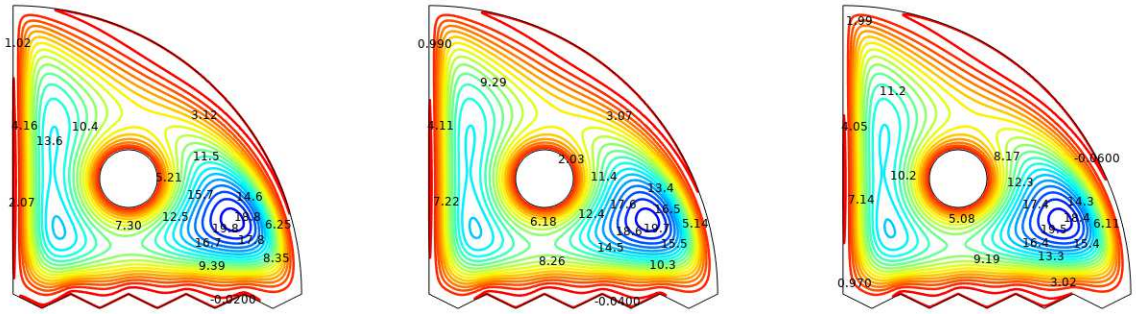
The thermal field evolution in Figure 7 is consistent with the changes in flow intensity. At $Ra = 10^3$, the isotherms are comparatively smooth and broadly distributed, indicating that heat transfer is primarily governed by conduction. A moderate deformation of the contours appears at $Ra = 10^4$ as buoyancy-induced circulation strengthens. At $Ra = 10^5$ and $Ra = 10^6$, the isotherms become markedly distorted and more closely packed near the cooled vertical wall and heated corrugated boundary, reflecting steeper temperature gradients and thinner thermal boundary layers. The simultaneous increase in $|\psi|_{\max}$ and distortion of the isotherms therefore indicates a progressive transition from conduction-controlled to convection-driven heat transfer with increasing Ra, resulting in enhanced convective thermal transport within the cavity.

4.3. Effect of Nanoparticle Volume Fraction

Figures 8 and 9 depict the changes in the flow and thermal characteristics resulting from variations in nanoparticle volume fraction ϕ at $Ra = 10^6$ and $Ha = 20$. Figure 8 reveals that the overall streamline topology remains nearly unchanged throughout the investigated range, with the principal circulation cells persisting around the circular obstacle. However, the flow intensity gradually decreases with increasing nanoparticle concentration. The maximum stream function magnitude, $|\psi|_{\max}$, decreases from approximately 20.4 at $\phi = 0$ to 20.2, 20.0, 19.8, 19.7, and 19.5 at $\phi = 0.01$, 0.02, 0.03, 0.04, and 0.05, respectively. Thus, increasing ϕ from 0 to 0.05 results in an overall reduction of approximately 4.4% in $|\psi|_{\max}$. This gradual weakening of the circulation can be attributed to the increase in effective viscosity, which enhances resistance to fluid motion and moderately suppresses buoyancy-driven convection.

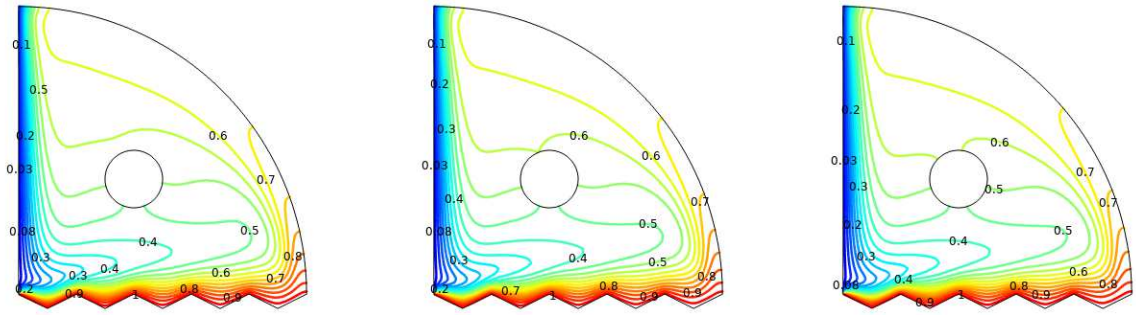


$\phi = 0.0$ $\phi = 0.01$ $\phi = 0.02$

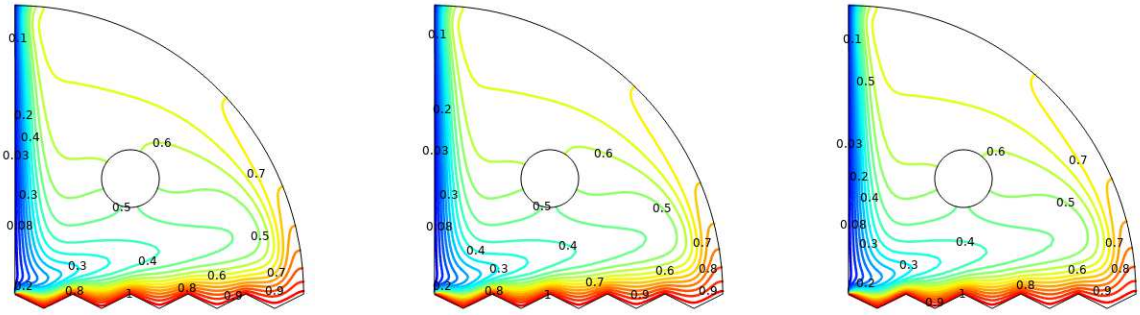


$\phi = 0.03$ $\phi = 0.04$ $\phi = 0.05$

Figure 8: Streamlines for different nanoparticle volume fractions at $Ha = 20$ and $Ra = 10^6$.



$\phi = 0.0$ $\phi = 0.01$ $\phi = 0.02$



$\phi = 0.03$ $\phi = 0.04$ $\phi = 0.05$

Figure 9: Isotherms for selected values of ϕ at $Ha = 20$ and $Ra = 10^6$.

The corresponding isotherms in Figure 9 exhibit only modest variations with increasing ϕ. Owing to the high Rayleigh number, the thermal contours remain distinctly distorted throughout the considered range, indicating the persistence of convection-dominated heat transport. Nevertheless, slight modifications are observed near the heated corrugated wall and around the circular obstacle as ϕ increases. These changes arise from the competing effects of enhanced effective thermal conductivity and increased viscous resistance. While nanoparticle addition promotes conductive heat transport, the associated increase in viscosity weakens fluid circulation. Consequently, increasing ϕ produces a relatively small alteration in the overall flow and thermal structures, characterized by a slight reduction in circulation strength together with enhanced conductive heat transport.

4.4 Average Nusselt Number

The effects of the governing parameters Ra, Ha, and ϕ on the average Nusselt number (Nu_{ave}) are presented in Figures (10-12). Figure 10 clearly shows that Nu_{ave} increases with Ra for all investigated Hartmann numbers, although the rate of enhancement becomes progressively weaker as Ha increases. At $Ha = 0$, Nu_{ave} rises from approximately 3.5 at $Ra = 10^3$ to 4.4, 6.3, and 9.4 at $Ra = 10^4$, $Ra = 10^5$, and $Ra = 10^6$, respectively. In contrast, at $Ha = 100$, it remains close to 3.5 at low Ra and reaches only about 5.6 at $Ra = 10^6$. This trend confirms that buoyancy-driven convection becomes increasingly dominant with increasing Ra, while a stronger magnetic field limits the associated enhancement in heat transfer.

The magnetic influence is more directly evident in Figure 11, where Nu_{ave} decreases continuously with increasing Ha, particularly at high Ra. At $Ra = 10^6$, increasing Ha from 0 to 100 reduces Nu_{ave} from approximately 9.4 to 5.6, corresponding to a decrease of about 40%. A similar but less pronounced reduction is observed at $Ra = 10^5$, whereas the curves at $Ra = 10^3$ and $Ra = 10^4$ remain comparatively insensitive to Ha. This behavior indicates that magnetic damping becomes more influential when buoyancy-induced circulation is strong. The Lorentz force generated by the applied magnetic field suppresses fluid motion and thermal mixing, thereby reducing convective heat transfer.

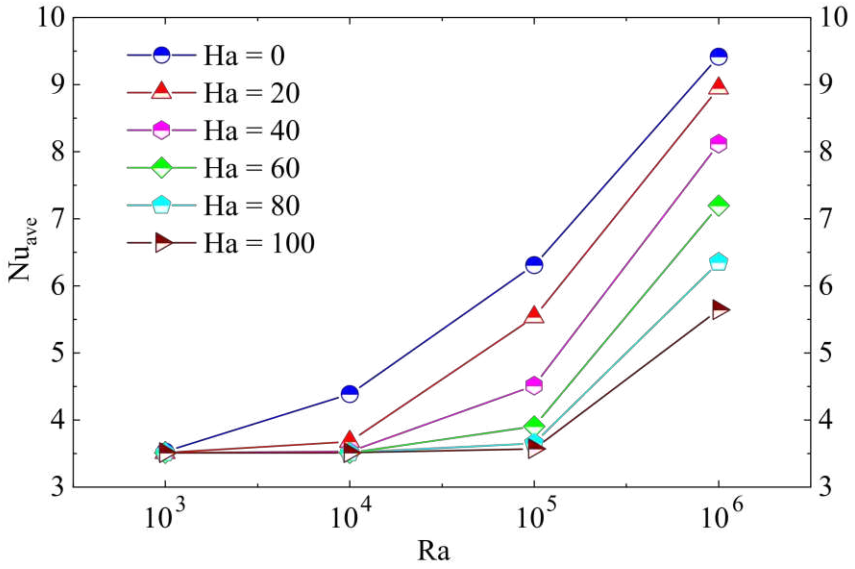


Figure 10: Influence of Ra and Ha on the average Nusselt number (Nu_{ave}) at $\phi = 0.05$.

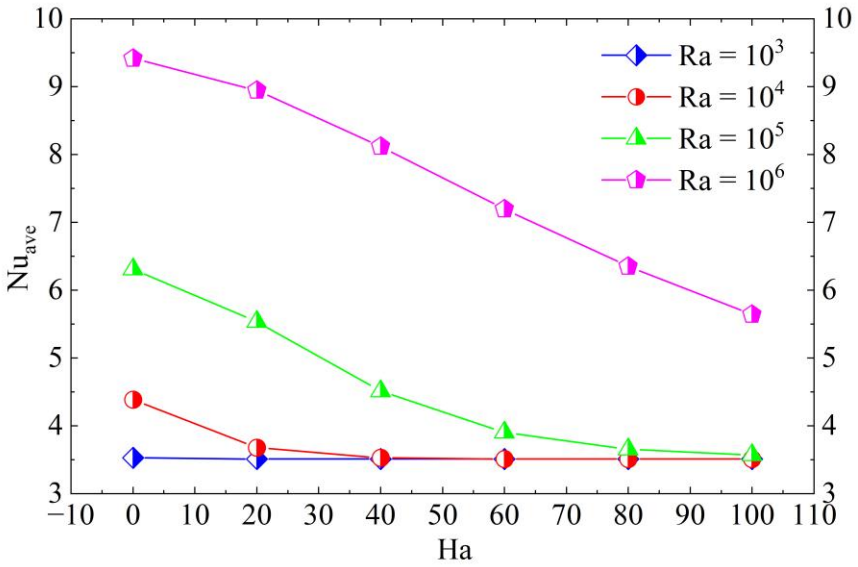


Figure 11: Average Nusselt number (Nu_{ave}) variation with Ha and Ra at $\phi = 0.05$.

Figure 12 shows the effect of nanoparticle volume fraction at $Ha = 20$. Unlike the suppressing influence of Ha, increasing ϕ produces a gradual rise in Nu_{ave} over the entire range of Ra. At $Ra = 10^6$, Nu_{ave} increases from approximately 8.3 at $\phi = 0$ to 8.9 at $\phi = 0.05$, while at $Ra = 10^5$ it increases from about 5.2 to 5.6. The enhancement is comparatively modest at lower Ra. This improvement is primarily associated with the increased effective thermal conductivity

of the nanofluid, which promotes heat transport despite the slight reduction in circulation caused by the increased viscosity. Overall, increasing Ra strongly enhances heat transfer, increasing Ha suppresses it through magnetic damping, whereas increasing ϕ provides a moderate improvement in Nu_{ave}.

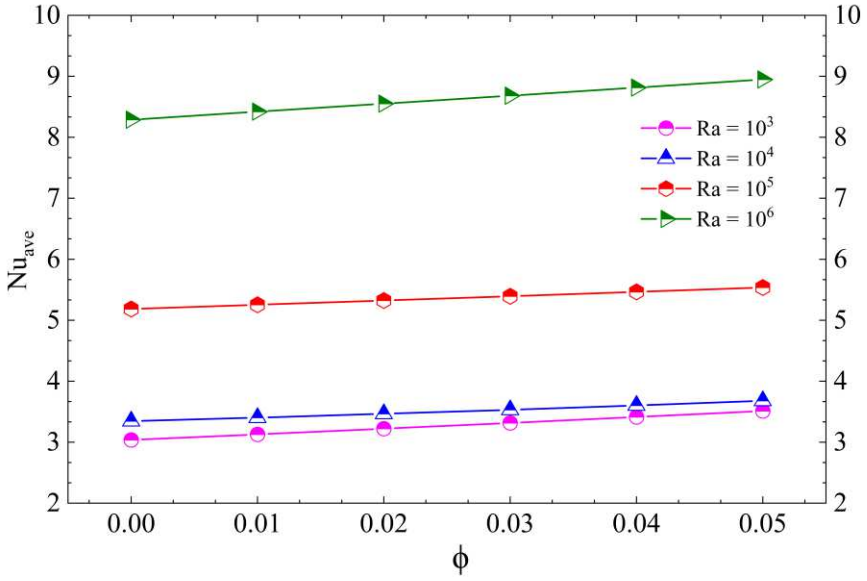


Figure 12: Variation of average Nusselt number (Nu_{ave}) against ϕ and Ra at $Ha = 20$.

5. Machine Learning Approach

The database was constructed from 151 CFD simulations, and subsequently used to train machine learning surrogate models for the average Nusselt number, Nu_{ave}, using the Rayleigh number (Ra), Hartmann number (Ha), and nanoparticle solid volume fraction (ϕ) as predictors. This section provides a detailed description of every sequential step followed in this study, such as the description, machine learning models, model training scheme, evaluation matrices, model performance comparison and SHAP analysis.

5.1 Dataset Description and Preprocessing

The Nu_{ave} distribution in Figure 13 shows positive skewness with most observations concentrated at relatively low values and a long tail extending toward higher heat transfer rates. This right-tailed distribution is physically consistent with the parametric design, that contains conduction-dominated, magnetically damped, and strongly buoyancy-driven heat transfer rates.

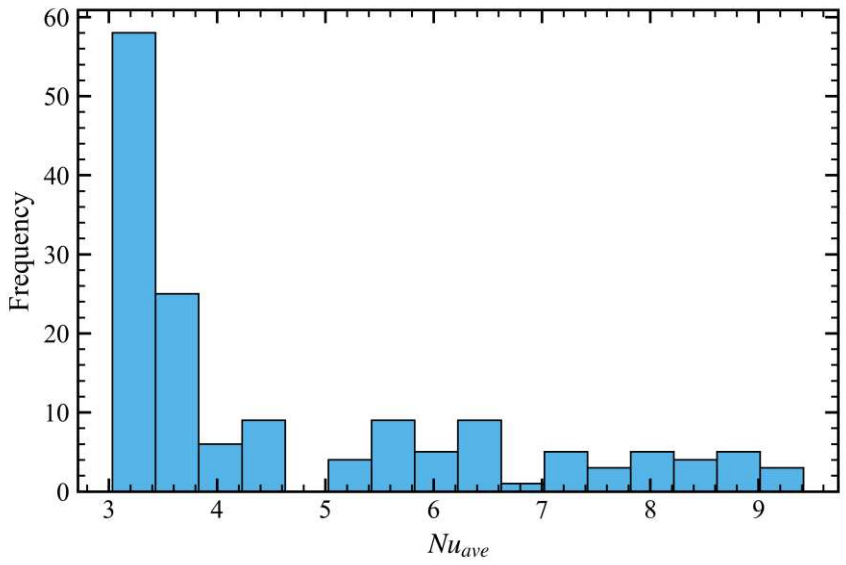


Figure 13: Distribution of average Nusselt number (Nu_{ave}) from the produced dataset.

To examine the linear dependence between the input parameters (Ra, Ha, ϕ) and the average Nusselt number (Nu_{ave}), the Pearson correlation coefficient was calculated as

$$r = \frac{\sum_{i=1}^{n}(x_i - \bar{x})(y_i - \bar{y})}{\sqrt{\left[\sum_{i=1}^{n}(x_i - \bar{x})^2\right]\left[\sum_{i=1}^{n}(y_i - \bar{y})^2\right]}}$$

where x_i and y_i denote the *ith* observations of two variables, $\bar{x}$ and $\bar{y}$ are the corresponding mean values calculated from N number of observations. The coefficient ranges from -1 to +1, where the sign indicates the direction and the magnitude represents the strength of linear dependency between the two parameters. The Pearson correlation coefficient matrix presented in Figure 14 reveals distinct linear relationships between the input parameters and average Nusselt number. A strong positive correlation is observed between Ra and Nu_{ave} with the Pearson correlation coefficient rank of 0.884, indicating that an increase in buoyancy strength generally consequently enhances heat transfer rate. In contrast to that, Ha shows a negative correlation with Nu_{ave} ($r = -0.330$), indicating the reduction in convective heat transfer rate associated with magnetic damping.

The nanoparticle volume fraction ϕ exhibits a comparatively weak positive linear correlation with Nu_{ave} ($r = 0.071$). Close to zero correlations among the input parameters (Ra, Ha, and ϕ) further indicate that the input parameters are linearly independent within the produced dataset. These results provide an initial description of the global linear trends and build the ground for the direction of analysis of the dataset for machine learning model training.

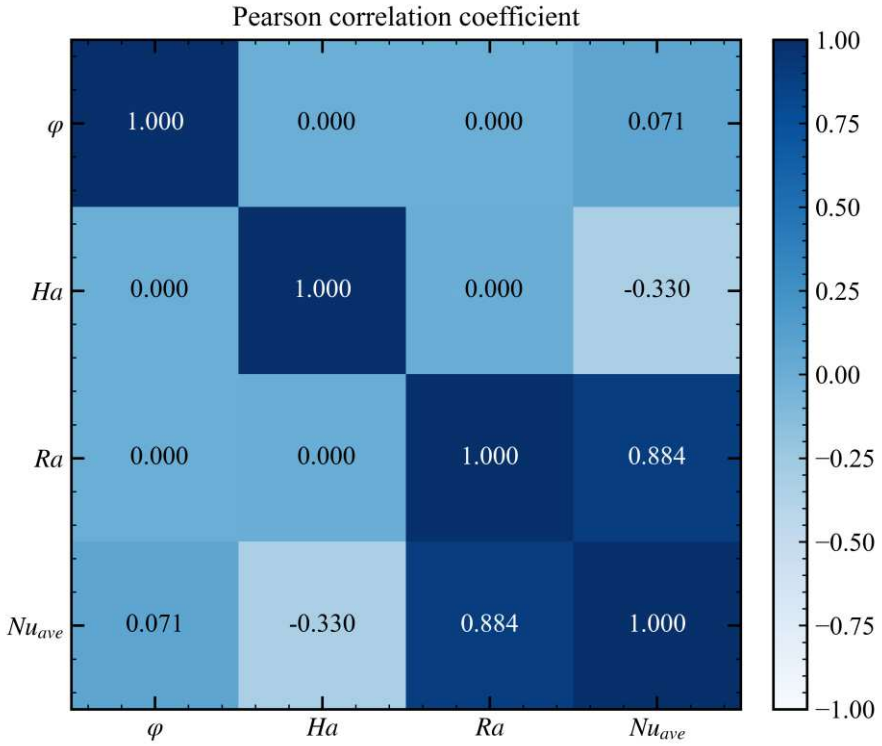


Figure 14: Pearson correlation heatmap for Ra, Ha, ϕ , and Nu_{ave} .

As gradient based machine learning models are sensitive to input feature scaling, each input features were normalized within the training portion of each cross-validation fold according to the z-score normalization as such

$$z = \frac{(x - \mu_{\text{train}})}{\sigma_{\text{train}}}$$

Where x is the sample from the dataset, μ_{train} is the mean of the feature calculated from the training fold, and σ_{train} is the standard deviation calculated from the training set.

5.2 Machine Learning Model Development

To develop a data-driven surrogate for the prediction of the average Nusselt number Nu_{ave}, four supervised machine learning models were trained namely Random Forest (RF), Extreme Gradient

Boosting (XGBoost), CatBoost (Categorical Boosting), and Artificial Neural Network (ANN). The Rayleigh number (Ra), Hartmann number (Ha), and nanoparticle volume fraction (ϕ) were used as input variables, while Nu_{ave} obtained from the CFD simulations was considered the target variable. These models were selected because of their established capability to capture nonlinear relationships and interactions from relatively small numerical datasets.

A five-fold cross validation strategy was employed for assessing generalization to unseen data and for reducing the dependence of the reported performance on a specific data split. The models were hyperparameter tuned through optuna, and were subsequently evaluated using the coefficient of determination (R^2), mean absolute error (MAE), mean square error (MSE), and root mean square error (RMSE).

5.2.1 Random Forest

Random Forest (RF) is an ensemble based supervised machine learning model that combines multiple decision trees to improve prediction accuracy and to reduce the variance associated with an individual tree. Each tree is constructed using a bootstrap sample of the training dataset, while a randomly selected subset of input features is considered at each split. For regression, the final prediction is obtained by averaging the outputs of all individual trees [43]:

$$\hat{y}_{\mathrm{RF}}(x) = \frac{1}{B}\sum_{b=1}^{B} T_b(x)$$

where $(\hat{y}_{RF}(x))$ is the prediction for the input vector (x), $(T_b(x))$ represents the prediction of the *bth* decision tree, and B denotes the total number of trees in the ensemble. The aggregation of independently trained trees generally improves model robustness and limits overfitting by reducing prediction variance.

5.2.2 XGBoost

Extreme Gradient Boosting (XGBoost) is an ensemble machine learning algorithm in which decision trees are constructed sequentially, with each successive tree trained to reduce the prediction errors of the preceding ensemble. In contrast to bagging based methods such as RF, XGBoost employs gradient boosting together with regularization to control model complexity and reduce overfitting [44]. The objective function at the *K-th* boosting stage can be expressed as

$$L = \sum_{i=1}^{N} l(y_i, \hat{y}_i) + \sum_{k=1}^{K} \Omega(f_k)$$

where $l(y_i, \hat{y}_i)$ represents the loss between the simulated value (y_i) and the predicted value $\hat{y}_i$, f_k denotes the *kth* regression tree, and $\Omega(f_k)$ is a regularization term that penalizes model complexity. The final prediction is obtained from the additive contribution of the sequentially constructed trees.

5.2.3 CatBoost

CatBoost is a gradient-boosting based machine learning algorithm that constructs an ensemble of decision trees sequentially with each new learner, introduced to minimize the residual error of the existing model. A distinguishing feature of CatBoost is its ordered boosting strategy, which reduces prediction bias during model training and improves generalization, particularly for small datasets [45]. The iterative boosting procedure may be represented as

$$F_m(x) = F_{m-1}(x) + \eta h_m(x)$$

where $F_m(x)$ is the updated ensemble prediction at iteration *m*, $F_{m-1}(x)$ represents the prediction from the previous iteration, $h_m(x)$ denotes the newly fitted decision tree, and η is the learning rate controlling the contribution of each successive tree.

5.2.4 Artificial Neural Network

Artificial Neural Network (ANN) is a machine learning approach inspired by interconnected biological neurons. A feed-forward ANN consists of an input layer, one or more hidden layers, and an output layer. Each neuron receives weighted signals from the preceding layer, adds a bias term, and transforms the resulting quantity using an activation function. For a hidden neuron, this operation can be expressed as [46]

$$h_j = g\left(\sum_{i=1}^{p} w_{ji} x_i + b_j\right)$$

where x_i represents the *ith* input variable, w_{ji} is the corresponding connection weight, b_j denotes the bias associated with the *jth* neuron, and *g(x)* is the activation function. The network parameters are iteratively adjusted during training by minimizing the difference between the predicted and simulated data.

5.3 Hyperparameter Tuning and Model Performance Evaluation

The hyperparameters of the RF, XGBoost, CatBoost, and ANN models were optimized within predefined search spaces to improve predictive performance and to control model complexity. The tuning procedure was performed on the data with the partition ratio of 80:20. The investigated hyperparameters, corresponding search ranges, and optimal values are summarized in Table 4.

Table 4: Hyperparameter tuning ranges and optimized values of the employed machine learning models for predicting Nu_{ave}

Model	Hyperparameter	Search space	Optimal value
Random Forest	n_estimators	200–900	600
	min_samples_split	2–12	4
	max_features	sqrt, log2, 1.0	1.0 (all)
XGBoost	learning_rate	0.01–0.20 (log scale)	0.1725
	n_estimators	120–520	460
	max_depth	2–5	3
	reg_lambda	0.001–20 (log scale)	7.690
CatBoost	depth	2–6	4
	learning_rate	0.01–0.18 (log scale)	0.1790
	l2_leaf_reg	0.01–50 (log scale)	23.568
	iterations	150–700	400
ANN	hidden-layer architecture	9 candidate architectures	(64, 32)
	learning_rate	2×10^{-4}–3×10^{-2} (log scale)	0.02104
	activation	ReLU, GELU, ELU	ELU
	dropout	0–0.12	0.05088

The predictive performance of the models was evaluated using coefficient of determination R^2, mean absolute error (MAE), mean square error (MSE), and root mean square error (RMSE). These metrics are mathematically defined as follows

$$R^2 = 1 - \frac{\sum_{i=1}^{N}\left(y_i - y_i'\right)^2}{\sum_{i=1}^{N}\left(y_i - \bar{y}\right)^2},\ MAE = \frac{1}{N}\sum_{i=1}^{N}\left|y_i - y_i'\right|,\ MSE = \frac{1}{N}\sum_{i=1}^{N}\left(y_i - y_i'\right)^2,\ RMSE = \sqrt{\frac{1}{N}\sum_{i=1}^{N}\left(y_i - y_i'\right)^2}$$

Here, y_i and y_i' represent the simulated and predicted values of Nu_{ave}, respectively, $\bar{y}$ is the mean of the distribution, and N denotes the number of samples. A higher R^2 and lower MAE, MSE, and RMSE indicate improved predictive performance.

5.4 Average Nusselt Number Prediction

The average Nusselt number, Nu_{ave}, was predicted using four machine learning models; CatBoost, XGBoost, Artificial Neural Network (ANN), and Random Forest (RF). The cross validation performances of the machine learning models are summarized in Table 5, while the agreement between the simulated and predicted Nu_{ave} for a representative fold is illustrated through the parity plots in Figure 16.

Table 5: Performance of the machine learning models for the prediction of Nu_{ave}

Model	CV RMSE	CV MSE	CV MAE	CV R^2
CatBoost	0.0488±0.0342	0.0033±0.0046	0.0270±0.0107	0.99883±0.00186
XGBoost	0.1089±0.0244	0.0123±0.0054	0.0797±0.0162	0.99573±0.00304
ANN	0.1606±0.0370	0.0269±0.0127	0.1224±0.0308	0.99090±0.00697
Random Forest	0.1791±0.0498	0.0341±0.0162	0.1063±0.0338	0.98825±0.00828

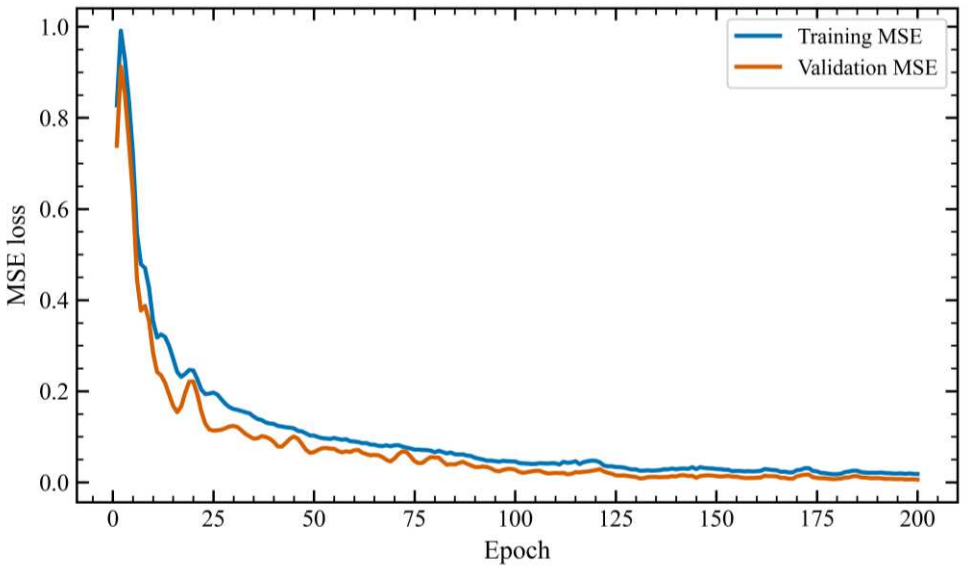


Figure 15: Training and validation MSE convergence of the compact ANN.

The ANN convergence curve in Figure 15 shows decreasing training and validation losses with increasing epochs, confirming stable convergence and reliable model performance.

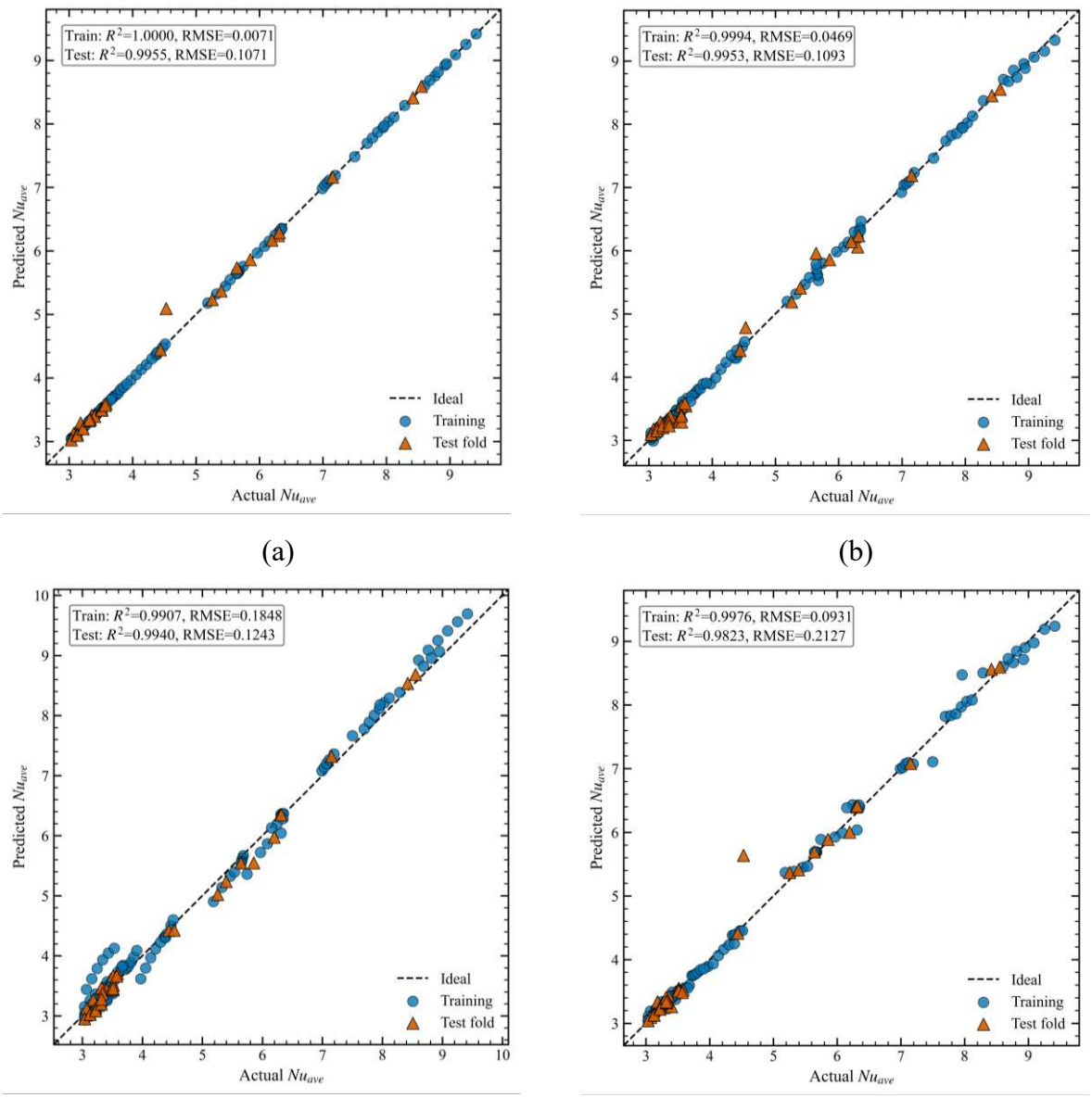


Figure 16: Parity plot of (a) CatBoost, (b) XGBoost, (c) ANN, and (d) Random Forest.

Among the four models, CatBoost achieved the best overall performance, with an RMSE of 0.0488±0.0342, MSE of 0.0033±0.0046, MAE of 0.0270±0.0107, and R^2 of 0.99883±0.00186. XGBoost showed the second highest accuracy, attaining an RMSE of 0.1089±0.0244 and R^2=0.99573±0.00304. ANN also provided satisfactory prediction performance with R^2=0.99090±0.00697, while RF exhibited the lowest R^2 of 0.98825±0.00828 and the highest RMSE of 0.1791±0.0498. Overall, CatBoost provided the most accurate prediction of Nu_{ave} followed by XGBoost. On the other hand, for the representative test fold, CatBoost achieved R^2

of 0.9955 and RMSE of 0.1071, closely followed by XGBoost with R^2 of 0.9953 and RMSE of 0.1093 as seen in Figure 16. ANN also showed good agreement with simulated ground truth data with R^2 of 0.9940, and RMSE of 0.1243, whereas RF exhibited comparatively greater scatter with R^2 of 0.9823, and RMSE of 0.2127. The predicted values from all four models generally follow the ideal line, with CatBoost and XGBoost showing the closest correspondence with the simulated results.

The comparative performance of the developed machine learning models based on five-fold cross validation is presented in Figure 17, where the error bars represent the standard error. The results demonstrate that CatBoost consistently provides the highest predictive accuracy, exhibiting the lowest RMSE, MAE and MSE values along with the highest R^2 among all evaluated models. XGBoost shows comparable performance and ranks second, whereas ANN and Random Forest exhibit relatively higher prediction errors and lower R^2 values.

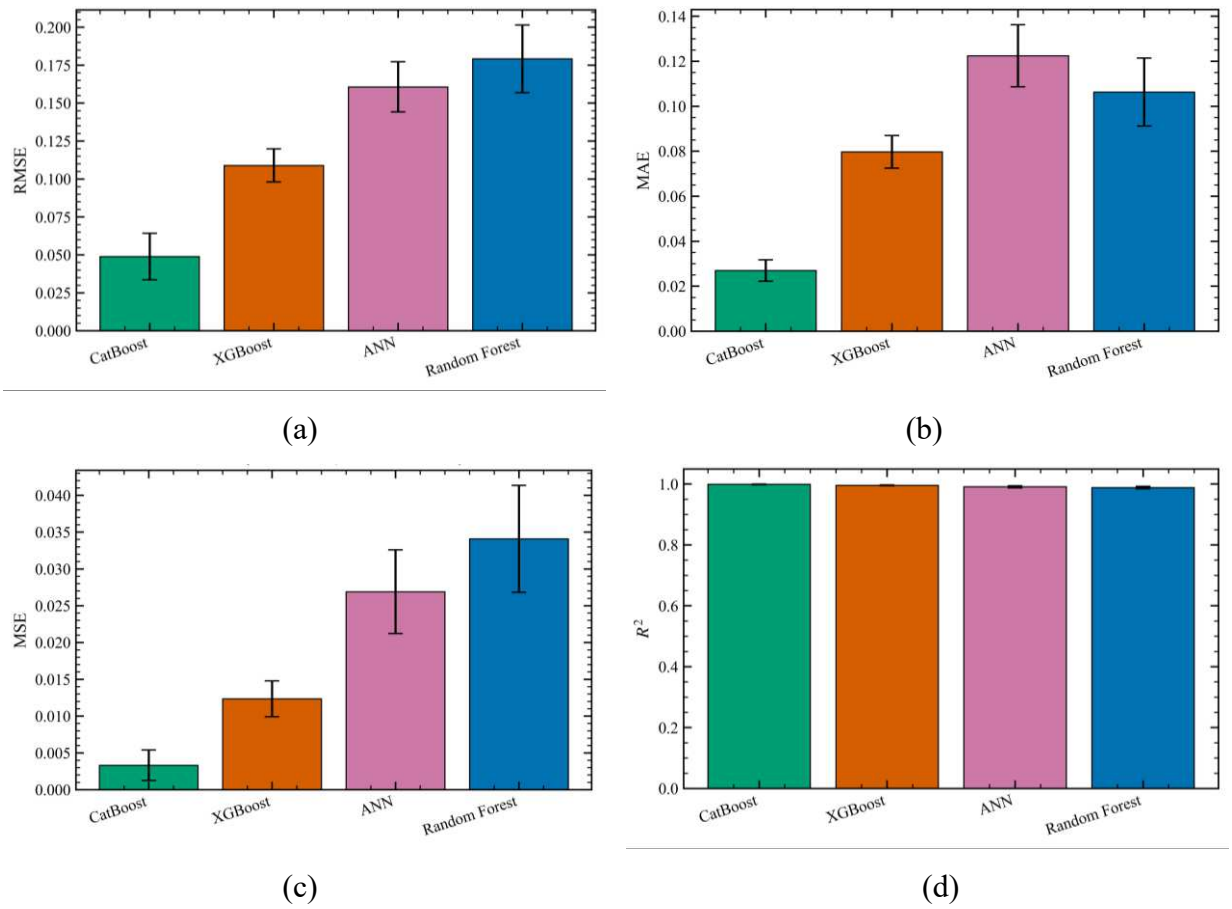


Figure 17: Comparison of the machine learning models on the basis of (a) RMSE, (b) MAE, (c) MSE and (d) R^2.

The small variation observed across the folds indicates the stability of the models, with CatBoost showing the most consistent predictive capability for Nu_{ave} estimation.

5.5 SHAP Importance for Nu_{ave}

The global importance of Ra, Ha, and ϕ was evaluated using the mean absolute SHapley Additive exPlanations (SHAP) values, as presented in Figure 18. All four models consistently identify Ra as the most influential parameter, followed by Ha and ϕ. The mean absolute SHAP values of Ra range from 1.428 to 1.447 across the models, while those of Ha vary between 0.533 and 0.544.

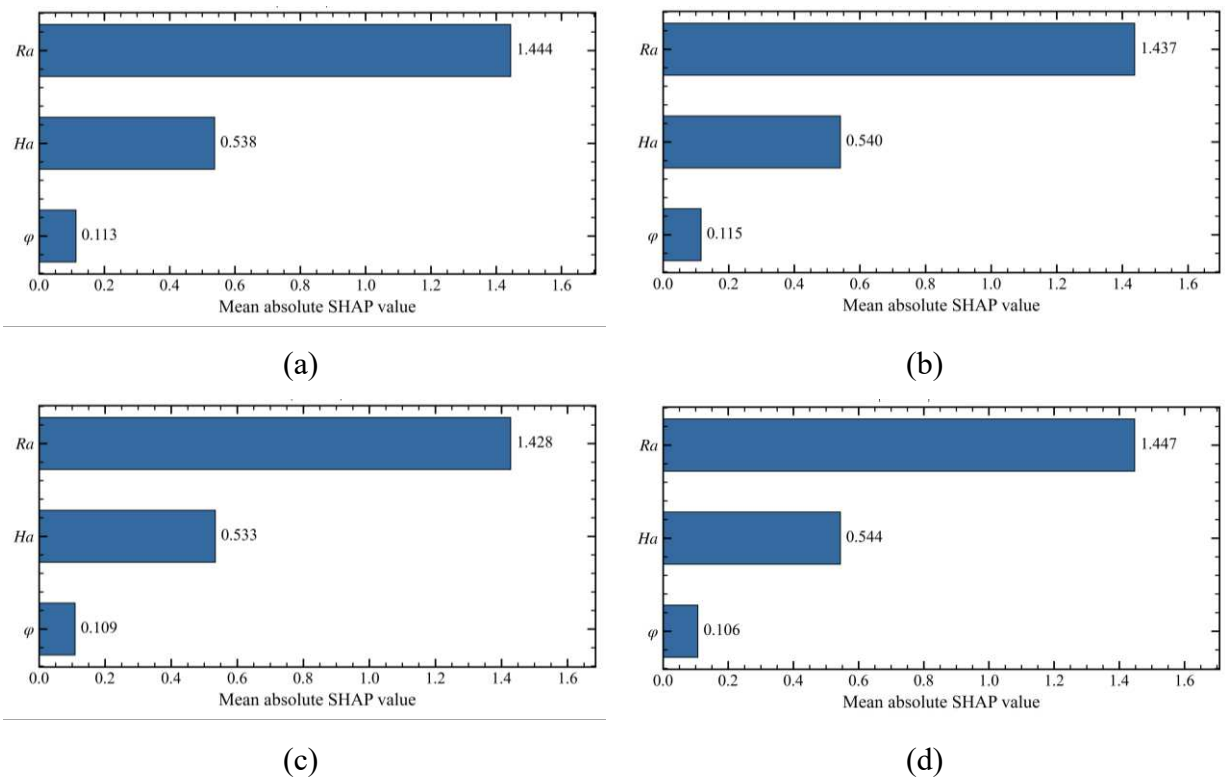


Figure 18: Mean absolute SHAP (global) explanations obtained for models (a) CatBoost, (b) XGBoost, (c) ANN, and (d) Random Forest.

In comparison, ϕ exhibits considerably lower values of 0.106-0.115. Therefore, a consistent feature importance order is obtained as Ra >Ha > ϕ. The dominant contribution of Ra indicates the strong influence of buoyancy on the heat transfer rate, whereas the second highest importance of Ha reflects the effect of magnetic damping. The substantially lower importance of ϕ indicates a comparatively smaller influence of nanoparticle concentration within the investigated range. The

agreement in feature ranking among all four models also supports the robustness of the identified parameter importance.

5.6 SHAP Beeswarm Analysis

The SHAP beeswarm plots shown in Figure 19 illustrate both the magnitude and direction of the influence of the governing parameters on Nu_{ave}. The feature values vary from low (blue) to high (red), while positive and negative SHAP values represent increasing and decreasing contributions to the predicted Nu_{ave}, respectively.

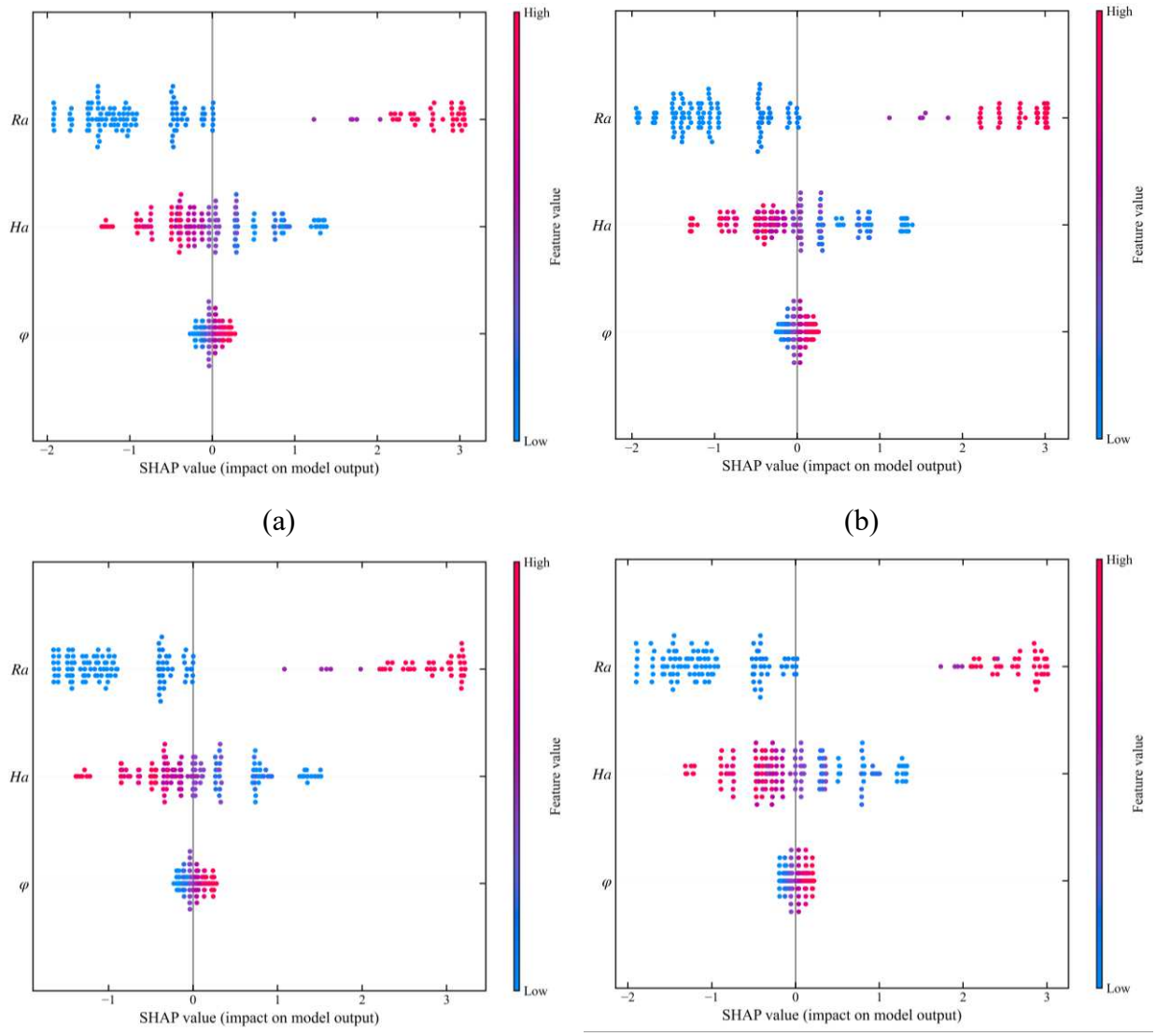


Figure 19: SHAP beeswarm plot for machine learning models (a) CatBoost, (b) XGBoost, (c) ANN, and (d) Random Forest.

Across all four models, higher Ra values are predominantly associated with positive SHAP values, whereas lower Ra values show negative contributions. This indicates a strong enhancement of Nu_{ave} with increasing Ra, consistent with the intensification of buoyancy driven convection.

An opposite behavior is observed for Ha. Higher Ha values are mainly associated with negative SHAP values, while lower values generally exhibit positive contributions. The trend reflects the suppression of convective heat transfer by the Lorentz force as the magnetic field strength increases. For ϕ, the SHAP values remain concentrated close to zero, confirming its comparatively smaller contribution. Nevertheless, higher ϕ values generally shift toward positive SHAP values, indicating a modest enhancement of Nu_{ave} with increasing nanoparticle volume fraction. Overall, the SHAP analysis consistently shows that Ra enhances the heat transfer response, Ha suppresses it, and ϕ exerts a weaker positive influence within the considered parameter range.

5.7 Comparison Between CFD Simulated Data and CatBoost Predictions

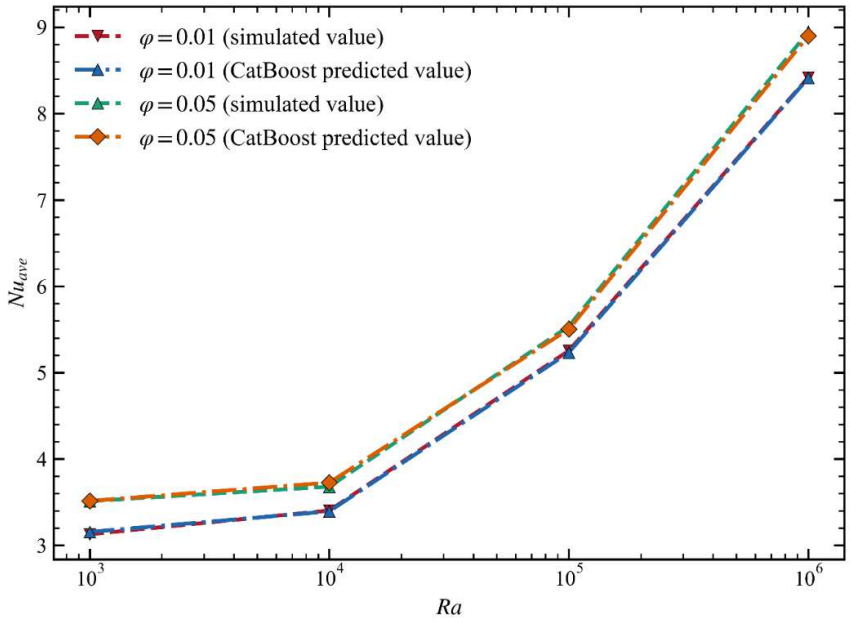


Figure 20: Comparison of CFD simulated data and CatBoost Predicted data for $Ha = 20$.

The accuracy of the CatBoost model was further evaluated by comparing with the CFD simulated average Nusselt numbers for $Ra = 10^3$ to $Ra = 10^6$ at $Ha = 20$ and nanoparticle volume fractions of $\phi = 0.01$ and $\phi = 0.05$ as shown in Figure 20. The average Nusselt number increases with increasing Ra, indicating a transition from conduction dominated to convection dominated heat transfer at higher Rayleigh numbers. For both nanoparticle concentrations, higher ϕ results in enhanced heat transfer due to the improved thermal conductivity of the nanofluid. The CatBoost predictions closely matches with the CFD results throughout the investigated Ra range, with nearly overlapping curves, confirming the capability of the model to capture the nonlinear thermal behavior.

6. Conclusion

A two-dimensional MHD natural convective Cu-H_2O nanofluid flow in a quarter-circular enclosure with an insulated circular obstacle was investigated using the Galerkin finite element method. A total of 151 numerical results were also used to develop machine learning models for predicting the average Nusselt number. The main findings are summarized as follows:

- At lower Ra, weak circulation and nearly parallel isotherms indicate conduction dominated heat transfer, whereas higher Ra produces stronger circulation and increasingly distorted isotherms, confirming the dominance of convection. Increasing Ha weakens the flow circulation due to magnetic damping.
- The average Nusselt number increases with Ra and nanoparticle volume fraction ϕ, while it decreases with increasing Ha.
- The highest average Nusselt number of 9.4159 is obtained at $Ra = 10^6$, $Ha = 0$, and $\phi = 0.05$.
- A dataset of 151 numerical results was used to train and evaluate XGBoost, CatBoost, Random Forest, and Artificial Neural Network models using five-fold cross validation.
- Among the four models, CatBoost provides the best predictive performance, with RMSE = 0.0488 ± 0.0342, MAE = 0.0270 ± 0.0107, MSE = 0.0033 ± 0.0046, and R^2 = 0.99883±0.00186.

- SHAP bar and beeswarm analyses identify Ra as the dominant parameter influencing the average Nusselt number prediction, while also revealing the relative contribution and impact trends of the remaining governing parameters.
- Overall, the proposed CFD-ML framework offers a reliable and efficient strategy for predicting heat transfer behaviour in complex MHD nanofluid systems while reducing the computational demand associated with repeated numerical simulations.

Data availability statement

The CFD dataset produced in this work is open-source and publicly available on Github: https://github.com/sadia-akter-jnu/MHD-machine-learning.

Funding Information

The authors declare that no funding was received for conducting this research or preparing the manuscript.

Acknowledgment

The authors gratefully acknowledge the computational facilities of the Department of Mathematics, Jagannath University, for completing this study.

References

1. Bawazeer, S. A. & Alsoufi, M. S. Natural convection in a square cavity: Effects of Rayleigh and Prandtl numbers on heat transfer and flow patterns. *Case Stud. Therm. Eng.* **73**, 106680 (2025).
2. Rahman, M. M., Öztop, H. F., Ahsan, A. & Orfi, J. Natural convection effects on heat and mass transfer in a curvilinear triangular cavity. *Int. J. Heat Mass Transf.* **55**, 6250–6259 (2012).
3. Aydin, O. & Yesiloz, G. Natural Convection in a Quadrantal Cavity Heated and Cooled on Adjacent Walls. *J. Heat Transfer* **133**, (2011).
4. Usman, M., Haq, R. U., Hamid, M., Lu, D. & Zhang, Z. Natural convection role in MHD flow of heat exchange inside a wavy cavity. *Int. Commun. Heat Mass Transfer* **159**, 108250 (2024).

5. Hasanuzzaman, M., Öztop, H. F., Rahman, M. M., Rahim, N. A., Saidur, R. & Varol, Y. Magnetohydrodynamic natural convection in trapezoidal cavities. *Int. Commun. Heat Mass Transfer* **39**, 1384–1394 (2012).
6. Pirmohammadi, M. & Ghassemi, M. Effect of magnetic field on convection heat transfer inside a tilted square enclosure. *Int. Commun. Heat Mass Transfer* **36**, 776–780 (2009).
7. Sarris, I. E., Kakarantzas, S. C., Grecos, A. P. & Vlachos, N. S. MHD natural convection in a laterally and volumetrically heated square cavity. *Int. J. Heat Mass Transf.* **48**, 3443–3453 (2005).
8. Ahmad, S., Cham, B. M., Liu, D., Islam, S. U., Hussien, M. A. & Waqas, H. Numerical analysis of heat and mass transfer of MHD natural convection flow in a cavity with effects of source and sink. *Case Stud. Therm. Eng.* **53**, 103926 (2024).
9. Sarala Devi, T., Venkata Lakshmi, C., Venkatadri, K. & Suryanarayana Reddy, M. Influence of external magnetic wire on natural convection of non-Newtonian fluid in a square cavity. *Partial Differ. Equ. Appl. Math.* **4**, 100041 (2021).
10. Aziz, T., Haq, R. U., Sadiq, M. A. & Bahaidarah, H. M. S. Thermal performance of MHD natural convection flow in a concentric semi-circle porous enclosure having corrugated radius. *Int. Commun. Heat Mass Transfer* **146**, 106905 (2023).
11. Haq, R. U., Soomro, F. A., Mekkaoui, T. & Al-Mdallal, Q. M. MHD natural convection flow enclosure in a corrugated cavity filled with a porous medium. *Int. J. Heat Mass Transf.* **121**, 1168–1178 (2018).
12. Bahmani, M., Babagoli, M., Jalili, P., Jalili, B. & Ganji, D. D. The numerical study on the MHD natural convection trend of square/circle corrugated porous media. *J. Eng. Res.* **13**, 1744–1754 (2025).
13. Choudhary, P., Kumar, A. & Kumar, R. Numerical study of magneto-hydrodynamics natural convective flow in a porous-corrugated enclosure using a higher-order compact finite difference scheme. *Int. Commun. Heat Mass Transfer* **156**, 107677 (2024).
14. Choudhary, P. & Ray, R. K. MHD natural convection flow in a porous medium-filled corrugated enclosure: Effect of heat sources with different heights. *Int. J. Therm. Sci.* **196**, 108673 (2024).
15. Choi, S. U. S. & Eastman, J. Enhancing thermal conductivity of fluids with nanoparticles (1995).

16. Islam, T., Alam, M. N., Niazai, S., Khan, I., Fayz-Al-Asad, M. & Alqahtani, S. Heat generation/absorption effect on natural convective heat transfer in a wavy triangular cavity filled with nanofluid. *Sci. Rep.* **13**, 21171 (2023).
17. Dutta, S., Pati, S. & Baranyi, L. Numerical analysis of magnetohydrodynamic natural convection in a nanofluid filled quadrantal enclosure. *Case Stud. Therm. Eng.* **28**, 101507 (2021).
18. Abdulkadhim, A. et al. Effect of heat generation and heat absorption on natural convection of Cu-water nanofluid in a wavy enclosure under magnetic field. *Int. Commun. Heat Mass Transfer* **120**, 105024 (2021).
19. Faraz, N., Shemyal Nisar, M., Khan, Y., Hussain, A. & Iqbal, K. Natural convection of Cu-H_2O nanofluid inside hexagonal enclosure fitted with a square cavity with a non-uniformly heated wall(s). *Results Phys.* **51**, 106648 (2023).
20. Mokhefi, A., Youcefi, S., Valdiserri, P. & Rossi di Schio, E. Magnetic field influence on the stabilization of an elastic fin under natural convection in a square cavity with nanofluids. *Therm. Sci. Eng. Prog.* **68**, 104258 (2025).
21. Uddin, M. J., Hasan, M. M. & Faroughi, S. A. Convective transport in a nanofluid-filled annulus with an eccentric hypocycloid within a square disk. *Int. J. Thermofluids* **22**, 100664 (2024).
22. Al-Farhany, K., Abdulkadhim, A., Hamzah, H. K., Ali, F. H. & Chamkha, A. MHD effects on natural convection in a U-shaped enclosure filled with nanofluid saturated porous media with two baffles. *Prog. Nucl. Energy* **145**, 104136 (2022).
23. Al-Farhany, K., Al-Chlaihawi, K. K., Al-dawody, M. F., Biswas, N. & Chamkha, A. J. Effects of fins on magnetohydrodynamic conjugate natural convection in a nanofluid saturated porous inclined enclosure. *Int. Commun. Heat Mass Transfer* **126**, 105413 (2021).
24. Alam, M. S., Billah, M. M., Hossain, S. M. C., Keya, S. S. & Haque, M. M. MHD influence on convective heat transfer in a semi-circular cavity using nonhomogeneous nanofluid model. *Int. J. Thermofluids* **16**, 100197 (2022).
25. Alaydamee, H. H., Alomari, M. A., Al-Salami, Q. H., Alyousuf, F. Q. A., Alqurashi, F. & Flayyih, M. A. Numerical analysis of unsteady free convection under the combined influence of inclined magnetohydrodynamic and exothermic chemical reaction in an enclosure filled with nanofluid. *Int. J. Thermofluids* **23**, 100704 (2024).

26. Roy, N. C., Rumpa, S. H. & Amin, A. Natural convective ternary nanofluid flow in a trapezoidal wavy enclosure with multiple cold obstacles. *Int. J. Heat Fluid Flow* **117**, 110139 (2026).
27. Selimefendigil, F. & Öztop, H. F. Natural convection and entropy generation of nanofluid filled cavity having different shaped obstacles under the influence of magnetic field and internal heat generation. *J. Taiwan Inst. Chem. Eng.* **56**, 42–56 (2015).
28. Tumse, S., Tantekin, A., Bilgili, M. & Sahin, B. Evaluation of heat transfer characteristics of a rectangular grooved heat exchanger under magnetic field using artificial neural network. *Int. J. Heat Fluid Flow* **112**, 109712 (2025).
29. Topolnicki, R., Dłotko, P. & Matyka, M. Physics informed convolutional neural networks for fluid flow through porous media. *Sci. Rep.* **16**, 27879 (2026).
30. Refaie Ali, A., Mahmood, R., Asghar, A., Majeed, A. H. & Behiry, M. H. AI-based predictive approach via FFB propagation in a driven-cavity of Ostwald de-Waele fluid using CFD-ANN and Levenberg–Marquardt. *Sci. Rep.* **14**, 11024 (2024).
31. Al-Zaitone, B., Ammar, T., Sami, A. H., Elshabrawy, M. & Kozal, M. Supervised machine learning approach to estimating the convective heat transfer coefficient for heated oblate spheroidal particles. *Int. J. Thermofluids* **30**, 101476 (2025).
32. Alkindi, S. M. et al. Heat transfer optimization in a fluid-filled porous hexagonal cavity using finite element modeling, artificial neural networks, and response surface methodology. *Therm. Sci. Eng. Prog.* **77**, 104871 (2026).
33. Hasan, M. S., Alam, M. N. & Sarker, M. M. A. MHD convective thermal performance in a nanofluid filled wavy enclosure: An artificial neural network model. *Int. J. Thermofluids* **27**, 101186 (2025).
34. Wang, T., Huang, Z., Sun, Z. & Xi, G. Reconstruction of natural convection within an enclosure using deep neural network. *Int. J. Heat Mass Transf.* **164**, 120626 (2021).
35. Ziaur, R. M., Azad, A. K., Nasir Uddin, M., Rahman, M. M. & Karim, M. F. Artificial neural network prediction on free convection in a triangular chamber with a V-shaped corrugated bottom wall filled with nanofluid. *Eng. Sci. Technol. Int. J.* **57**, 101824 (2024).
36. Bawazeer, S. A., Alhamayani, A., Al-lehaibi, M. & Alsoufi, M. S. Data-driven machine learning prediction of Nusselt number in fin-enhanced natural convection within square cavities. *Therm. Sci. Eng. Prog.* **74**, 104702 (2026).

37. Reddy, N. K., Swamy, H. A. K., Kang, Y., Sankar, M. & Do, Y. Integrating machine learning with numerical simulations of magneto-convective flow and irreversibility dynamics in a partially porous cavity with hot blocks. *Case Stud. Therm. Eng.* **75**, 107242 (2025).
38. Ahmad, H. et al. Numerical and machine learning based evaluation of ethylene glycol based hybrid nano-structured (TiO_2-SWCNTs) fluid flow. *Sci. Rep.* **15**, 6084 (2025).
39. Ashique, A., Afzal, U., Masood, K., Shah, N. A. & Chung, J. D. FEM and XGBoost investigation of three-dimensional magnetohydrodynamic mixed convection in a cone-cubic enclosure with internal heat generation. *Case Stud. Therm. Eng.* **84**, 108343 (2026).
40. Cremades, A., Hoyas, S. & Vinuesa, R. Additive-feature-attribution methods: A review on explainable artificial intelligence for fluid dynamics and heat transfer. *Int. J. Heat Fluid Flow* **112**, 109662 (2025).
41. Brinkman, H. C. The viscosity of concentrated suspensions and solutions. *J. Chem. Phys.* **20**, 571 (1952).
42. Maxwell, J. C. A Treatise on Electricity and Magnetism. Cambridge University Press, Cambridge (2010; originally published 1873).
43. Breiman, L. Random forests. *Mach. Learn.* **45**, 5-32 (2001).
44. Chen, T. & Guestrin, C. XGBoost: A scalable tree boosting system. In Proceedings of the 22nd ACM SIGKDD International Conference on Knowledge Discovery and Data Mining (ACM, San Francisco, CA, USA, 2016).
45. Prokhorenkova, L., Gusev, G., Vorobev, A., Dorogush, A. V. & Gulin, A. CatBoost: unbiased boosting with categorical features. In Proceedings of the 32nd International Conference on Neural Information Processing Systems (2018).
46. Rumelhart, D. E., Hinton, G. E. & Williams, R. J. Learning representations by back-propagating errors. *Nature* **323**, 533–536 (1986).

Supplementary Files

This is a list of supplementary files associated with this preprint. Click to download.

- Highlights.docx